The Astrophysical Journal Supplement Series, 181:360–390, 2009 April doi:10.1088/0067-0049/181/2/360

STAR FORMATION ACTIVITY OF CORES WITHIN INFRARED DARK CLOUDS

E. T. Chambers[1], J. M. Jackson[1], J. M. Rathborne[2], and R. Simon[3]
[1] Institute for Astrophysical Research, Boston University, Boston, MA 02215, USA; etc1@bu.edu, jackson@bu.edu
[2] Harvard-Smithsonian Center for Astrophysics, Cambridge, MA 02138, USA; jrathborne@cfa.harvard.edu
[3] I.Physikalisches Institut, Universität zu Köln, 50937 Köln, Germany; simonr@ph1.uni-koeln.de
Received 2008 September 18; accepted 2009 January 7; published 2009 March 11

ABSTRACT

Infrared Dark Clouds (IRDCs) contain compact cores which probably host the early stages of high-mass star formation. Many of these cores contain regions of extended, enhanced 4.5 μm emission, the so-called "green fuzzies," which indicate shocked gas. Many cores also contain 24 μm emission, presumably from heated dust which indicates embedded protostars. Because "green fuzzies" and 24 μm point sources both indicate star formation, we have developed an algorithm to identify star-forming cores within IRDCs by searching for the simultaneous presence of these two distinct indicators. We employ this algorithm on a sample of 190 cores found toward IRDCs, and classify the cores as "active" if they contain a green fuzzy coincident with an embedded 24 μm source, and as "quiescent" if they contain neither IR signature. We hypothesize that the "quiescent" cores represent the earliest "preprotostellar" (starless) core phase, before the development of a warm protostar, and that the "active" cores represent a later phase, after the development of a protostar. We test this idea by comparing the sizes, densities, and maser activity of the "active" and "quiescent" cores. We find that, on average, "active" cores have smaller sizes, higher densities, and more pronounced water and methanol maser activity than the "quiescent" cores. This is expected if the "quiescent" cores are in an earlier evolutionary state than the "active" cores. The masses of "active" cores suggest that they may be forming high-mass stars. The highest mass "quiescent" cores are excellent candidates for the elusive high-mass starless cores.

Key words: dust, extinction – ISM: clouds – masers – stars: formation

1. INTRODUCTION

The early stages of high-mass star formation are poorly understood. Because high-mass stars and protostars are rare and evolve over short timescales, finding bona fide high-mass protostars in their earliest stages is difficult. Although only a handful of these objects have been found (e.g., Beuther et al. 2005; Rathborne et al. 2005), recent observations and theory (e.g., Zinnecker & Yorke 2007) suggest that they should be found within cores which are dense ($n_{\rm H_2} > 10^5$ cm^{-3}), cold (10 K $< T <$ 20 K), and massive ($\sim$100 $M_\odot$). Recently, a new class of molecular clouds containing cores with these properties was discovered–the infrared dark clouds (IRDCs). These cores within IRDCs may well host the earliest stages of high-mass star formation.

IRDCs were discovered by the *ISO* and *MSX* surveys as dark extinction regions of high contrast against the bright Galactic mid-infrared background (Perault et al. 1996; Carey et al. 1998; Hennebelle et al. 2001). Early studies of IRDCs (e.g., Egan et al. 1998; Carey et al. 1998, 2000) found them to be both cold ($T < 25$ K) and dense ($n_{\rm H_2} > 10^5$ cm^{-3}). The detection of strong mm (Beuther et al. 2005; Rathborne et al. 2005, 2006) and (sub)mm (Lis & Carlstrom 1994; Carey et al. 2000; Redman et al. 2003; Rathborne et al. 2005) dust emission from cores within IRDCs, combined with their cold temperatures and high densities, make IRDCs ideal candidates in which to search for the earliest stages of high-mass star formation. Some studies have indeed shown that high-mass stars are forming within these cores (e.g., Beuther et al. 2005; Rathborne et al. 2005, 2007; Pillai et al. 2006).

We have embarked on a systematic, multiwavelength study of IRDCs. Using *MSX* 8 μm images, we have created a catalog of 10,931 IRDCs (Simon et al. 2006a). The LSR velocities of 313 of these IRDCs were determined using morphological matching of the ^{13}CO (1–0) line emission in a particular channel from the Boston University-Five College Radio Astronomy Observatory (BU-FCRAO) Galactic Ring Survey (GRS; Jackson et al. 2006) with the *MSX* 8 μm extinction features (Simon et al. 2006b). Using these velocities, Simon et al. (2006b) calculated kinematic distances to the IRDCs using the Galactic rotation curve of Clemens (1985). At the galactocentric radii of these IRDCs ($R_{\rm GC} > 3$ kpc for all 313 IRDCs), the choice of the rotation curve has a little effect on the calculated distances. Indeed, using a flat rotation curve (Θ_o =220 km s^{-1}) in place of the Clemens (1985) rotation curve results in only minor differences in the calculated distances. Because IRDCs are seen in silhouette, the kinematic distance ambiguity in the inner Galaxy is solved by assuming that the IRDCs are located at the near kinematic distance. With the kinematic distances, Simon et al. (2006b) then derived the sizes ($\sim$5 pc) and masses ($\sim 10^3$ $M_\odot$) of IRDCs. We select the darkest 38 of these IRDCs for further study. These 38 IRDCs all have contrasts (flux decrement relative to the background in *MSX* 8 μm images; see Simon et al. 2006a) $> 36\%$ and lie within $15^\circ < \ell < 55^\circ$ and $|b| < 1^\circ$.

Using the Institute de Radioastronomie Millemetrique (IRAM) 30 m telescope, Rathborne et al. (2006) mapped these 38 IRDCs in 1.2 mm continuum emission and found 190 cores, with 140 identified as cold ($T \approx 15$ K) and compact ($R \lesssim 15''$). These cold, compact cores have typical sizes and masses of $\sim$0.5 pc and $\sim$120 $M_\odot$. These sizes and masses are smaller than the sizes and masses of cluster-forming clumps (10^2–10^3 $M_\odot$, $\sim$1 pc, which are typical of IRDCs themselves; Lada & Lada 2003; Motte et al. 2003) but larger than hot and cold cores which will form individual stars (1–100 $M_\odot$, $<$0.1 pc; Myers & Benson 1983; Ward-Thompson et al. 1994; Garay & Lizano 1999). Thus, it is possible that some cores within IRDCs may form more than one star. Indeed, interferometric (sub)mm observations show that some cores

within IRDCs do contain multiple protostellar condensations (Rathborne et al. 2007, 2008). Nevertheless, in this paper, we will call the objects identified in the IRAM 30 m observations (Rathborne et al. 2006) cores to differentiate them from the clump-like IRDCs which contain them.

In order to further study and characterize the earliest stages of (high-mass) star formation, it is important to find criteria that allow for a discrimination of (sub)mm cores into (1) preprotostellar, starless cores and (2) protostellar cores in which star formation has commenced.

1.1. Active and Quiescent Cores

In this paper, we propose a method which uses two IR criteria to determine which cores within IRDCs are in a quiescent, preprotostellar state and which cores are in an active, protostellar state. Here we present this method along with tests to probe its validity.

The first of the IR criteria is the detection of a slightly extended region of enhanced 4.5 μm emission. This method relies on Galactic Legacy Infrared Mid-Plane Survey Extraordinaire (GLIMPSE; Benjamin et al. 2003) mid-IR (3–8 μm) *Spitzer* images obtained with the Infrared Array Camera (IRAC; Fazio et al. 2004). It was initially thought that, as their name suggests, IRDCs were completely devoid of IR emission. However, the improved sensitivity and angular resolution of GLIMPSE over earlier Galactic IR surveys, such as *MSX*, reveal that some cores within IRDCs do indeed contain previously undetected mid-IR emission. The relative strength of this emission varies across the four IRAC bands. In mid-IR 3-color images with 8.0 μm emission displayed in red, 4.5 μm emission in green, and 3.6 μm emission in blue, many of these cores reveal extended regions of "green" emission (i.e., enhanced emission at 4.5 μm). We call these regions "green fuzzies." It has been postulated that this enhanced 4.5 μm emission is due to shock-excited spectral line emission, either the H_2 0-0 $S(9)$ line at 4.69 μm (e.g., Noriega-Crespo et al. 2004) or the CO $v = 1$–0 rovibrational bandhead at 4.5–5 μm (e.g., Marston et al. 2004). Regardless of the specific spectral carrier, the "green fuzzies" almost certainly trace shocked gas. If this is indeed correct, then the detection of "green fuzzies" indicates that there are shocks, and thus probably outflows driven by star formation, within these cores. Indeed, both Beuther et al. (2005) and Rathborne et al. (2005) find "green fuzzies" associated with high-mass protostars within cores found in IRDCs.

Although highly extincted stars may also appear green in these 3-color images due to the flattening of the extinction law between 4.5 μm and 8.0 μm (Indebetouw et al. 2005), it is unlikely that the "green fuzzies" are simply extincted background stars. Unlike stars, the "green fuzzies" are extended. Moreover, the high extinction seen toward IRDCs ($A_v \gtrsim 100$ mag) would make a background star difficult to detect.

To help rule out this possibility, we use a second IR criterion as a proxy for star formation. This criterion requires the detection of a 24 μm point source in images obtained with the Multiband Imaging Photometer for *Spitzer* (MIPS; Rieke et al. 2004). The improved sensitivity and angular resolution of *Spitzer*/MIPS allow for the detection and separation of embedded sources not possible with earlier surveys, such as *MSX* or *IRAS*. Bright 24 μm emission traces material accreting from the core onto the central protostar, converting gravitational energy into thermal energy, thereby heating the dust in the center of the core. The heated dust radiates its energy via gray body radiation, which peaks either in the (sub)mm regime (for cold, starless cores) or the far-IR regime (for warmer, protostellar cores). Because the cores are optically thin at these wavelengths, this radiation is able to escape the core. Consequently, embedded protostars manifest themselves as unresolved 24 μm point sources associated with dense cores. Thus, when we detect a 24 μm point source, we take this as indirect evidence that an accreting protostar within the core gives rise to this emission. Cores which do not contain an accreting protostar remain cold, with dust temperatures too low to emit detectable 24 μm emission. As a result, the detection of a 24 μm point source coincident with a core is a signpost for active star formation within that core.

Because both "green fuzzies" and 24 μm point sources indicate active star formation, we classify a core within an IRDC which contains both indicators coincident with each other as an "active core"; when a core contains neither IR indicator, we classify it as a "quiescent core." We also find cores which contain either a "green fuzzy" or a 24 μm point source, but not both. We call these cores "intermediate cores." We hypothesize that "intermediate cores" represent a transition phase between the active and quiescent cores. Because these cores contain only one of the two IR star-forming criteria in our algorithm, to be conservative we exclude the intermediate cores from most of the further analysis in this paper.

We find that IRDCs harbor both active and quiescent cores. We hypothesize that the active cores are currently forming stars, some of which may be high mass, while the quiescent cores are starless, currently devoid of detectable IR star formation activity. We test this hypothesis by comparing the sizes, densities, and maser activity between the active and quiescent cores.

If active cores condense from quiescent cores, they should be smaller and denser. To test this hypothesis, we examine the physical sizes of active and quiescent cores to determine whether active cores are indeed smaller. We also probe the density of active and quiescent IRDC cores by calculating the mean density of the cores using their sizes and masses. If our hypothesis is correct, then active cores should be denser than quiescent cores.

We also test the star formation activity of all 190 cores using maser emission, a well-known signpost of star formation. Both H_2O masers at 22.23 GHz and the Class I CH_3OH masers at 24.96 GHz are found toward star-forming regions and are formed in shocks and outflows, with collisions pumping the population inversion. If active cores are forming stars, then they should preferentially contain masers, while the quiescent cores should not.

In this paper, we present our algorithm for the identification of "green fuzzies" and our classification scheme for cores within IRDCs. Using the aforementioned tests, we find that active cores are smaller, denser, and much more likely to contain H_2O and CH_3OH maser emission than quiescent cores. The observational evidence therefore supports the idea that protostars within IRDCs can be identified by the detection of green fuzzies correlated with 24 μm point sources, and that IRDCs are indeed the birthplaces of stars, at least some of which are high mass.

2. DATA AND OBSERVATIONS

We examine the star formation activity within 190 compact 1.2 mm continuum cores identified by Rathborne et al. (2006). These 190 cores were found toward 38 IRDCs which have known kinematic distances. Rathborne et al. (2006) separated these 190 cores into two categories: "warm" cores with associated *MSX* 8 μm emission, and "cold" cores unassociated with *MSX* 8 μm emission. The better angular resolution of the

Table 1
Summary of Observations

Telescope	Instrument	Wavelength/ Frequency	Angular Resolution (″)	1σ rms noise
Spitzer	MIPS[a]	24 μm	7.1	0.12 mJy
	IRAC[b]	3.6 μm	1.1	0.27 MJy sr^{-1}
	IRAC	4.5 μm	1.3	0.25 MJy sr^{-1}
	IRAC	5.8 μm	1.7	0.61 MJy sr^{-1}
	IRAC	8.0 μm	2.4	0.37 MJy sr^{-1}
GBT	GBT Spectrometer	22.23 GHz	34	56 mK
	GBT Spectrometer	24.96 GHz	30	43 mK

Notes.
[a] MIPS sensitivities use the SENS-PET tool with a high background.
[b] IRAC sensitivities use the SENS-PET tool with a low background.

Spitzer/IRAC GLIMPSE data, however, reveals that several of the "warm" cores were spuriously identified, since at the 2″ angular resolution of *Spitzer*, the 8 μm emission is clearly offset from the core. Because of this possible *MSX* misidentification, we retain all 190 compact 1.2 mm cores in our analysis.

We present results from a combination of many datasets (see Table 1), including both continuum and spectral line observations.

2.1. Continuum Observations

The 3.6, 4.5, 5.8, and 8.0 μm images were obtained by the *Spitzer Space Telescope* as part of the GLIMPSE survey (Benjamin et al. 2003). This survey employed the use of IRAC and the data were processed by the GLIMPSE team.

The *Spitzer*/MIPS instrument was used to obtain 24 μm images. Of the 38 IRDCs, 30 were imaged in the raster mapping mode. The map sizes were either 3 rows × 3 columns (14′ × 14′) or 5 rows × 5 columns (19′ × 19′), depending on the size of the IRDC, with half-array spacing. The maps were obtained with 3 s exposures and 3 cycles, yielding an extended source sensitivity of 0.129 MJy sr^{-1} and a point source sensitivity of 124 μJy (1σ; using the online SENS-PET tool). The MIPS data were processed using the standard *Spitzer* Science Center data processing pipeline. For the remaining eight clouds, we use 24 μm images from the MIPSGAL survey (Carey et al. 2005). The data were processed by the MIPSGAL team and have an extended source sensitivity of 0.205 MJy sr^{-1} and a point source sensitivity of 207 μJy (1σ; using the online SENS-PET tool).

2.2. Spectroscopic Observations

An H_2O and CH_3OH maser survey of all 190 cores was carried out using the Robert C. Byrd Green Bank Telescope (GBT) of the National Radio Astronomy Observatory. The two transitions observed were the $6(1,6) - 5(2,3)$ $F = 5 - 4$ H_2O maser line at 22.235 GHz and the 5(2,3)−5(1,4) E CH_3OH maser line at 24.959 GHz. The approximate beam size is 33″ at the H_2O maser frequency, and 30″ at the CH_3OH maser frequency. Observations were made using the GBT Spectrometer and the 22–26 GHz *K*-band receiver in 2006 December and 2007 January. Spectra were taken using the in-band frequency switching mode with a frequency switch of 4 MHz, a total bandwidth of 12.5 MHz, and a velocity resolution of 0.04 km s^{-1}. Typical rms noise values ($T_{\rm rms}$) for the H_2O and CH_3OH spectra are 0.07 K and 0.06 K per channel, respectively. Regular pointing and focus checks were made throughout the observations. The two in-band frequency switched spectra for each pointing were averaged together, and first-order baselines were removed using the GBTIDL software package (Garwood et al. 2005). To be considered a detection, the peak of the detected maser line must be $\geqslant 3T_{\rm rms}$. For the faintest sources, an additional boxcar smoothing of several channels was applied when necessary to improve the signal to noise. Because the GBT beam size (∼30″) is often comparable to the separation between multiple cores within the same IRDC, individual maser features in these cases were often detected multiple times. If a single-maser feature is detected in the spectra of several closely spaced positions, it is assigned to the core toward which the maser feature is brightest.

3. RESULTS

In order to classify the star formation activity in these cores, we have developed an algorithm to identify "green fuzzies" and a scheme to classify cores within IRDCs based solely on *Spitzer* IR observations. Sections 3.1 and 3.2 describe this algorithm and its application to our sample of 190 cores. Sections 3.3 describes the results of our H_2O and CH_3OH maser survey.

3.1. IRAC Classification

In IRAC 3-color images (with the 8.0 μm emission displayed in red, 4.5 μm in green, and the 3.6 μm in blue), most objects have either "red" (flux steadily rising with wavelength, e.g., H II regions) or "blue" (flux steadily falling with wavelength, e.g., unextincted stars) colors. "Green" (flux enhanced in the 4.5 μm band) objects are rarer and fall into two main categories: (1) extincted stars, and (2) extended objects typically found toward regions of shocked gas. Because the 4.5 μm green enhancement in the extended regions is likely shock excited, and because IRDCs are purported to harbor the earliest stages of star formation (including high-mass stars), the detection of "green fuzzies" toward IRDCs should indicate star formation activity within these cores. With this in mind, we have developed an automated algorithm to identify green fuzzies in the GLIMPSE database. This algorithm, the Green Fuzzy Finder (GFF; see Appendix A for a detailed description of the algorithm), finds contiguous pixels which meet specific criteria for mid-IR colors, fluxes, and angular sizes. The values describing these criteria were determined by iterating until the algorithm recovered most of the green fuzzies identified by eye, while simultaneously minimizing the identification of spurious features. Our algorithm defines green fuzzies as regions in the GLIMPSE database that meet the following color criteria: (1) the 4.5 μm to 3.6 μm flux ratio must be $\geqslant 1.8$, (2) the 4.5 μm to 5.8 μm flux ratio must be $\geqslant 0.40$, and (3) the 4.5 μm to 8.0 μm flux ratio must be $\geqslant 0.45$. In addition, to ensure that the selected regions are significant detections, we also require an absolute 5σ flux threshold in the 4.5 μm band, $F_{4.5\mu m} \geqslant 1.26$ MJy sr^{-1}. Finally, in order to avoid confusion with heavily extincted stars, we require the green fuzzies to be extended. The FWHM diameter of the point spread function (PSF) for stellar sources in each of the IRAC bands is ∼2″ (with a pixel size of 1.″2; Fazio et al. 2004), so we require that green fuzzies contain at least nine contiguous pixels ($d \gtrsim 3.''6$) which satisfy the color and flux threshold criteria.

We ran the GFF algorithm over the extent of each of the 38 IRDCs in our study. The boundaries of the IRDC were defined using 3σ (30 mJy beam^{-1}) contours of 1.2 mm continuum emission as determined by Rathborne et al. (2006). Having identified all the green fuzzies within the IRDCs, we then determined whether any of the green fuzzies were associated

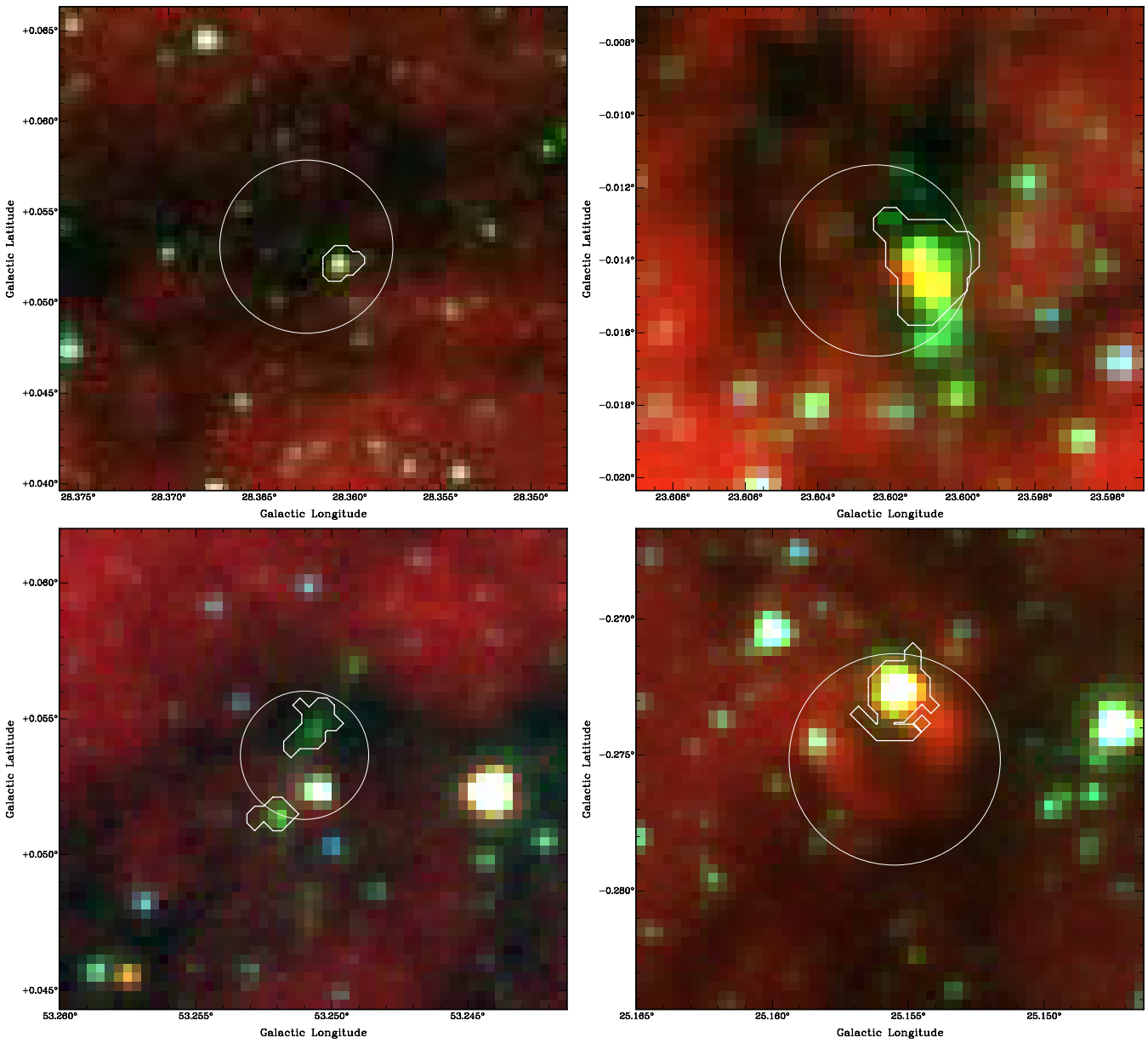

Figure 1. IRAC 3-color (8.0 μm in red, 4.5 μm in green, 3.6 μm in blue) images of cores containing green fuzzies. The circles mark the position and angular size of the cores, while the white contours show the boundaries of the green fuzzies.

with the cores. We select green fuzzies to be associated with a core if they have at least one pixel that falls within the core's boundary, as defined by its center position and radius (Rathborne et al. 2006). Thus, a single core may contain more than one green fuzzy, but each green fuzzy may only be assigned to one core. In the rare case that a green fuzzy lies within the boundaries of two or more cores, it is assigned to the nearest (smallest angular separation) core. Figure 1 shows the green fuzzies found toward four cores. We find a total of 57 green fuzzies in 47 cores (10 cores contain two green fuzzies).

In addition to green fuzzies, the GLIMPSE database reveals other objects detected in the mid-IR by IRAC that fall within the boundaries of the cores, but do not meet the required selection criteria to be identified as a green fuzzy. We can further classify these objects based on their IRAC colors. In a similar fashion as the GFF, we employ an automated algorithm (described in Appendix B) to identify these cores. Cores associated with bright ($\geqslant 25\sigma$) 8.0 μm emission sources are classified as "red," and cores associated with bright ($\geqslant 25\sigma$) 3.6 μm emission sources are classified as "blue" (see Figure 2). If a core is associated with both bright 8.0 μm and 3.6 μm emission, then the brighter of the two bands determines if the core is "red" or "blue." In all, 35 of our sample of 190 cores are associated with bright 8 μm emission ("red" cores). Many of these "red" cores are probably H II regions, ionized by OB stars which formed within the IRDC. A total of six cores are associated with bright 3.6 μm emission ("blue").

Because our algorithm associates cores with IRAC sources based only on their positional coincidence, it is entirely possible that our classification scheme associates cores with unrelated IR emission sources along the same line of sight. For example, every "blue" core is coincident with a bright, compact blue source that is probably a foreground star. Moreover, because H II regions would tend to have "red" colors in the IRAC bands

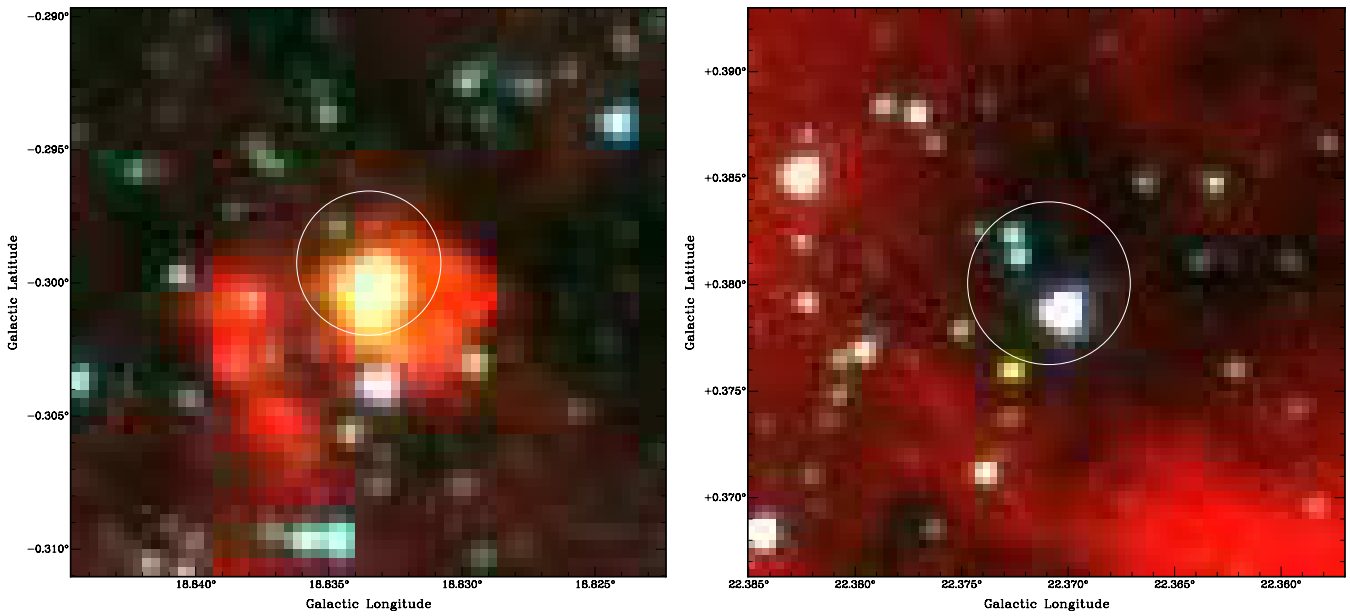

Figure 2. IRAC 3-color (8.0 μm in red, 4.5 μm in green, 3.6 μm in blue) images of a red core (left) and a blue core (right). The circles mark the position and angular size of the cores.

due to emission from polycyclic aromatic hydrocarbons (PAHs) and heated dust, compact H II regions along the line of sight may be aligned by chance with a core. Because IRDCs are parts of larger molecular clouds and are located in the crowded Galactic plane, it is common to find warm, mm-bright, star-forming cores in close proximity to the IRDCs. Thus, some of the "red" cores could possibly be chance alignments of H II regions and cores within our sample. Indeed, several of these cores appear to lie outside the darkest extinction regions in the IRDC.

After identifying the cores containing green fuzzies, as well as the "red," and "blue" cores, about half of our sample of cores (102 out of 190) remain unassociated with any extended IRAC emission. To summarize, of the 190 cores examined here, 47 (25%) contain green fuzzies, 35 (18%) contain red sources, six (3%) contain blue sources, and 102 (54%) contain no bright IRAC emission. Table 2 lists all cores in our sample, using the same naming convention as Rathborne et al. (2006) (Columns 1 and 2). Columns 3 and 4 list the coordinates of each core (Rathborne et al. 2006). If a core contains a green fuzzy, the central position (the average ℓ and b values of the green fuzzy pixels) of the green fuzzy is listed. Column 5 contains the IRAC classification of each core. Cores which contain no significant detectable IRAC emission are labeled "None," cores which contain a green fuzzy are labeled "G.F.," red (8 μm emission) cores are labeled "red," and blue (3.6 μm emission) cores are labeled "blue." Figure 3 displays IRAC 3-color images of each of the 38 IRDCs and all 190 cores in our sample. The circles mark the positions and sizes of the cores, and the boxes mark the positions of the green fuzzies.

3.2. 24 μm Emission

In order to determine which cores contain embedded protostars, we search for 24 μm point sources within our sample of 190 cores. We find that 98 cores contain 24 μm point sources within their boundaries (see Appendix C for the 24 μm point source detection algorithm). Figure 3 displays MIPS 24 μm images of the 38 IRDCs which contain all 190 cores. As with the IRAC images, the circles mark the positions and sizes of the cores, and the boxes mark the positions of the green fuzzies.

Since both green fuzzies, which indicate shocks, and 24 μm point sources, which indicate protostars, trace star formation in the core, they ought to be associated with each other. We tested this idea by searching for 24 μm point sources within the boundaries of the green fuzzy established by the GFF. As expected, green fuzzies and 24 μm point sources are closely associated. Specifically, we find that 74% of green fuzzies are associated with a 24 μm point source. Of the remaining 12 green fuzzies not associated with 24 μm emission, three are in cores which do contain another green fuzzy that is associated with a 24 μm point source. Table 2 lists the 24 μm flux measured toward each core which has a significant detection ($\geqslant 20\sigma$, see Appendix C). Table 3 shows the correlation between 24 μm emission and the different IRAC classifications.

We now classify all 190 cores based on their IR emission characteristics. We choose to separate the cores into five specific classes: quiescent cores, intermediate cores, active cores, red cores, and blue cores. The quiescent cores contain no significant IRAC or 24 μm emission (Figure 4). Intermediate cores contain either a green fuzzy or a 24 μm point source, but not both. Active cores contain a green fuzzy coincident with a 24 μm point source (Figure 4). Finally, red cores contain a region of 8 μm emission, while blue cores contain a region of bright 3.6 μm emission. Table 4 summarizes this classification scheme.

3.3. H_2O and CH_3OH Masers

Because maser emission is a well-known signpost of star formation, we can pinpoint regions of star formation in cores within IRDCs by searching for associated maser emission. We detected H_2O masers toward 67 cores and CH_3OH masers toward 15 cores (Figures 5 and 6). Toward many of the cores, we detect several distinct H_2O maser velocity components. Although only a few CH_3OH masers were detected, 14 of these cores (93%) associated with CH_3OH masers also contain H_2O masers. Columns 7 and 8 in Table 2 list the detections of H_2O and CH_3OH masers, respectively. Table 3 shows the

Table 2
Properties of Cores within IRDCs

IRDC	Core	ℓ[a] (°)	b[a] (°)	IRAC Classification	24 μm Flux (mJy)	H_2O Maser	CH_3OH Maser	Mass[b] ($M_\odot$)
(1)	(2)	(3)	(4)	(5)	(6)	(7)	(8)	(9)
MSXDC G015.05+00.07								
	MM1	15.0058	0.0092	None	···	···	···	105
	MM2	15.0552	0.0832	Red	131	···	···	83
	MM3	15.0872	0.0894	None	···	···	···	22
	MM4	15.0743	0.1298	None	···	···	···	43
	MM5	15.0429	0.0756	None	···	···	···	29
MSXDC G015.31−00.16								
	MM1	15.2578	−0.1557	Red	166	···	···	38
	MM2	15.2712	−0.1212	None	16	···	···	101
	MM3	15.2813	−0.0926	None	···	···	···	164
	MM4	15.2512	−0.1211	None	···	···	···	18
	MM5	15.2765	−0.1125	None	···	···	···	32
MSXDC G018.82−00.28								
	MM1	18.7348	−0.2258	None	41	Y	Y[c]	887
	MM2	18.8335	−0.2993	Red	514	···	···	242
	MM3	18.7009	−0.2278	G.F.	176	···	···	233
	MM4	18.7902	−0.2857	None	9	···	···	263
	MM5	18.8058	−0.3028	None	3[d]	···	···	170
	MM6	18.7999	−0.2940	None	···	···	···	205
MSXDC G019.27+00.07								
	MM1	19.3115	0.0674	Blue	144	Y	Y[c]	113
	MM2	19.2868	0.0839	G.F.	23	Y	···	114
MSXDC G022.35+00.41								
	MM1	22.3750	0.4466	G.F.	13	Y	Y[e]	253
	MM2	22.3444	0.4307	Red	100	···	···	215
	MM3	22.3709	0.3801	Blue	···	···	···	114
MSXDC G022.73+00.11								
	MM1	22.7273	0.1257	None	···	···	···	149
MSXDC G023.60+00.00								
	MM1	23.5687	0.0135	G.F.	214	Y	Y	365
	MM1	23.5693	0.0104	G.F.	37	Y	Y	365
	MM2	23.6010	−0.0141	G.F.	1058	Y	···	233
	MM3	23.5761	0.0239	Red	···	···	···	266
	MM4	23.6025	−0.0227	Red	38[d]	···	···	350
	MM5	23.5810	0.0314	G.F.	···	···	···	98
	MM6	23.5858	−0.0092	None	···	···	···	96
	MM7	23.6162	−0.0068	None	198	Y	···	286
	MM8	23.6227	−0.0211	None	···	···	···	45
	MM9	23.6354	−0.0034	None	···	···	···	80
MSXDC G024.08+00.04								
	MM1	24.1837	0.1208	Red	689	Y	···	196
	MM2	24.1414	0.1263	None	···	···	···	201
	MM3	24.1642	0.0865	None	···	···	···	124
	MM4	24.1573	0.0811	None	···	···	···	115
	MM5	24.1689	0.0648	None	···	···	···	87
MSXDC G024.33+00.11								
	MM1	24.3282	0.1450	Red	999	Y	Y	1759
	MM2	24.3432	0.0291	None	6	···	···	123
	MM3	24.3480	0.0622	Red	7[d]	···	···	126
	MM4	24.3173	0.0858	None	···	···	···	446
	MM5	24.3533	0.0375	None	3[d]	Y	···	192
	MM6	24.3355	0.1497	None	6	···	···	293
	MM7	24.2618	0.1017	None	···	···	···	93
	MM8	24.3239	0.0707	None	···	Y	···	305
	MM9	24.3359	0.0625	Red	1319	···	···	273
	MM10	24.3593	0.0681	None	15	Y	···	97
	MM11	24.3096	0.1484	None	···	···	···	275
MSXDC G024.60+00.08								
	MM1	24.6332	0.1537	G.F.	342	···	···	192
	MM2	24.6314	0.1728	None	13	Y	···	483
	MM3	24.6366	0.1520	G.F.	···	Y	Y	35
	MM4	24.6279	0.1542	None	···	···	···	27

Table 2
(Continued)

IRDC	Core	ℓ[a] (°)	b[a] (°)	IRAC Classification	24 μm Flux (mJy)	H_2O Maser	CH_3OH Maser	Mass[b] ($M_\odot$)
(1)	(2)	(3)	(4)	(5)	(6)	(7)	(8)	(9)
MSXDC G025.04−00.20								
	MM1	25.1554	−0.2729	G.F.	195	Y	···	276
	MM2	25.1656	−0.3049	None	7	Y	···	104
	MM3	25.1531	−0.2764	None	···	···	···	47
	MM4	25.1528	−0.2929	None	3	···	···	307
	MM5	25.1565	−0.2830	None	···	···	···	50
MSXDC G027.75+00.16								
	MM1	27.7415	0.1710	G.F.	42	···	···	320
	MM2	27.7455	0.1143	None	···	Y	···	133
	MM3	27.7417	0.1880	None	7	···	···	281
	MM4	27.7959	0.1523	None	···	···	···	123
	MM5	27.7726	0.1721	None	···	···	···	92
MSXDC G027.94−00.47								
	MM1	27.9683	−0.4745	Red	985	Y	Y	70
	MM2	27.9760	−0.4682	None	94	···	···	42
MSXDC G027.97−00.42								
	MM1	27.9719	−0.4219	G.F.	39	···	···	57
	MM2	28.0110	−0.4264	Red	207	Y	···	62
	MM3	27.9794	−0.4282	None	···	···	···	45
MSXDC G028.04−00.46								
	MM1	28.0472	−0.4563	G.F.	352	···	···	80
MSXDC G028.08+00.07								
	MM1	28.0879	0.0694	None	5	···	···	374
MSXDC G028.10−00.45								
	MM1	28.1082	−0.4461	None	···	···	···	78
	MM2	28.1101	−0.4516	None	···	···	···	19
MSXDC G028.23−00.19								
	MM1	28.2735	−0.1641	None	···	···	···	705
	MM2	28.2826	−0.1492	G.F.	···	···	···	108
	MM3	28.2818	−0.1565	None	···	···	···	38
MSXDC G028.28−00.34								
	MM1	28.2879	−0.3636	Red	···	Y	Y	411
	MM2	28.3041	−0.3847	Red	799[d]	Y	···	321
	MM3	28.2822	−0.3591	Red	820[d]	Y	···	68
	MM4	28.2867	−0.3472	G.F.	20[d]	···	···	139
MSXDC G028.37+00.07								
	MM1	28.4027	0.0828	G.F.	22	Y	Y[c]	1148
	MM1	28.3976	0.0804	G.F.	26	Y	Y[c]	1148
	MM2	28.3374	0.1169	None	1090	Y	Y[c]	542
	MM3	28.3219	−0.0103	Red	220	Y	···	482
	MM4	28.3473	0.0593	G.F.	45	Y	···	329
	MM5	28.3255	0.1613	Red	848	Y	···	177
	MM6	28.3576	0.0742	G.F.	4	Y	···	232
	MM6	28.3559	0.0699	G.F.	8	Y	···	232
	MM7	28.2924	0.0064	Red	28[d]	Y	···	304
	MM8	28.2445	0.0126	Red	802[d]	···	···	414
	MM9	28.3243	0.0676	None	···	···	···	397
	MM10	28.3605	0.0522	G.F.	22	Y	Y	358
	MM11	28.3535	0.1029	G.F.	17	···	···	447
	MM12	28.3279	−0.0390	None	···	···	···	476
	MM13	28.4191	0.1337	G.F.	···	···	···	463
	MM14	28.3563	0.0565	None	···	···	···	36
	MM15	28.3396	0.1423	Red	165	Y	···	134
	MM16	28.3675	0.1202	None	···	Y	···	447
	MM17	28.3876	0.0380	None	···	···	···	198
	MM18	28.4166	−0.0074	Red	390	Y	···	162
MSXDC G028.53−00.25								
	MM1	28.5654	−0.2351	None	···	···	···	1165
	MM2	28.5556	−0.2257	G.F.	16	···	···	2115
	MM3	28.5433	−0.2371	None	···	···	···	2044
	MM4	28.5589	−0.2413	None	···	Y	···	800
	MM5	28.5265	−0.2504	None	6	Y	···	234
	MM6	28.5574	−0.2383	None	···	Y	···	119
	MM7	28.5379	−0.2759	None	···	···	···	508

Table 2
(Continued)

IRDC	Core	ℓ[a] (°)	b[a] (°)	IRAC Classification	24 μm Flux (mJy)	H_2O Maser	CH_3OH Maser	Mass[b] ($M_\odot$)
(1)	(2)	(3)	(4)	(5)	(6)	(7)	(8)	(9)
	MM8	28.5431	−0.2653	None	···	···	···	185
	MM9	28.5899	−0.2286	None	4	···	···	166
	MM10	28.5790	−0.2305	None	···	Y	···	433
MSXDC G028.67+00.13								
	MM1	28.6882	0.1781	Red	2317	···	···	143
	MM2	28.6613	0.1455	None	31	···	···	394
	MM3	28.5786	0.1441	G.F.	317	···	···	122
	MM4	28.7168	0.1455	Blue	4	···	···	116
	MM5	28.6504	0.1259	None	···	···	···	103
	MM6	28.6467	0.1142	None	3[d]	···	···	113
	MM7	28.6436	0.1373	None	···	···	···	87
MSXDC G030.14−00.06								
	MM1	30.1448	−0.0672	G.F.	21	···	···	597
	MM2	30.1077	−0.0688	None	···	···	···	83
MSXDC G030.57−00.23								
	MM1	30.6490	−0.2029	G.F.	···	Y	Y[c]	419
	MM2	30.5302	−0.2591	Red	1341	···	···	198
	MM3	30.5828	−0.2125	None	7	···	···	257
	MM4	30.5769	−0.2497	None	···	···	···	300
	MM5	30.5965	−0.2307	None	···	···	···	144
	MM6	30.5630	−0.2456	None	11	···	···	104
MSXDC G030.97−00.14								
	MM1	30.9723	−0.1422	G.F.	2089	Y	···	417
	MM2	30.9843	−0.1354	None	···	Y	···	231
MSXDC G031.02−00.10								
	MM1	31.0249	−0.1085	Blue	···	···	···	349
MSXDC G031.97+00.07								
	MM1	32.0443	0.0589	G.F.	769	Y	Y[e]	1890
	MM2	32.0361	0.0573	None	···	Y	···	929
	MM3	32.0177	0.0652	None	···	Y	···	1222
	MM4	32.0114	0.0586	None	9	···	···	852
	MM5	31.9453	0.0768	None	7	···	···	178
	MM6	32.0273	0.0574	None	···	···	···	1181
	MM7	31.9826	0.0654	None	···	Y	···	290
	MM8	31.9978	0.0673	G.F.	192	···	···	493
	MM9	32.0243	0.0718	None	···	···	···	151
MSXDC G033.69−00.01								
	MM1	33.7398	−0.0192	Red	199	Y	···	1135
	MM2	33.6537	−0.0217	Red	3317	Y	···	1342
	MM3	33.6371	−0.0344	Red	637	Y	···	288
	MM4	33.7443	−0.0010	G.F.	18	Y	···	820
	MM5	33.6340	−0.0208	G.F.	864	Y	···	243
	MM5	33.6318	−0.0232	G.F.	···	Y	···	243
	MM6	33.6220	−0.0323	None	···	···	···	395
	MM7	33.7610	−0.0051	Blue	14	···	···	641
	MM8	33.7105	−0.0113	None	···	···	···	588
	MM9	33.7195	−0.0264	None	504	···	···	119
	MM10	33.6684	−0.0272	None	···	···	···	114
	MM11	33.7228	−0.0158	None	···	···	···	100
MSXDC G034.43+00.24								
	MM1	34.4111	0.2352	G.F.	1718	Y	Y[e]	1187
	MM2	34.4012	0.2270	Red	1401	Y	Y[c]	1284
	MM3	34.4597	0.2507	G.F.	···	Y	Y	301
	MM3	34.4604	0.2474	G.F.	129	Y	Y	301
	MM4	34.3965	0.2233	G.F.	111	Y	···	253
	MM4	34.3932	0.2209	G.F.	148	Y	···	253
	MM5	34.3873	0.2150	G.F.	4[d]	···	···	664
	MM6	34.4477	0.2508	None	5	···	···	126
	MM7	34.4384	0.2475	None	8	Y	···	87
	MM8	34.4246	0.2481	G.F.	6	···	···	108
	MM9	34.4537	0.2548	None	···	···	···	157
MSXDC G034.77−00.55								
	MM1	34.7122	−0.5947	Red	1211	···	Y	166
	MM2	34.7827	−0.5684	None	···	···	···	188

Table 2
(Continued)

IRDC	Core	ℓ[a] (°)	b[a] (°)	IRAC Classification	24 μm Flux (mJy)	H_2O Maser	CH_3OH Maser	Mass[b] ($M_\odot$)
(1)	(2)	(3)	(4)	(5)	(6)	(7)	(8)	(9)
	MM3	34.7340	−0.5671	None	3	···	···	14
	MM4	34.7845	−0.5609	None	···	···	···	70
MSXDC G035.39−00.33								
	MM1	35.4565	−0.1802	Red	602	Y	···	76
	MM2	35.4169	−0.2839	G.F.	251	Y	···	45
	MM3	35.4521	−0.2952	Red	2839	Y	···	79
	MM4	35.4849	−0.2840	G.F.	5	···	···	108
	MM4	35.4850	−0.2897	G.F.	3[d]	···	···	108
	MM5	35.4835	−0.2955	None	···	···	···	118
	MM6	35.4964	−0.2864	G.F.	28	···	···	71
	MM7	35.5258	−0.2707	G.F.	16	···	···	96
	MM7	35.5187	−0.2732	G.F.	57	···	···	96
	MM8	35.4912	−0.2831	None	···	···	···	59
	MM9	35.4777	−0.3097	None	···	···	···	42
MSXDC G035.59−00.24								
	MM1	35.6033	−0.2036	Red	319	···	···	65
	MM2	35.6006	−0.2333	G.F.	12	Y	···	48
	MM3	35.6084	−0.2418	G.F.	23	···	···	41
MSXDC G036.67−00.11								
	MM1	36.6661	−0.1133	None	···	···	···	49
	MM2	36.6412	−0.1073	None	···	···	···	58
MSXDC G038.95−00.47								
	MM1	38.9554	−0.4657	G.F.	···	···	···	117
	MM1	38.9569	−0.4694	G.F.	···	···	···	117
	MM2	38.9366	−0.4579	Red	1238	···	···	73
	MM3	38.9709	−0.4589	None	···	···	···	11
	MM4	38.9464	−0.4412	G.F.	227	Y	···	48
MSXDC G048.65−00.29								
	MM1	48.6715	−0.3044	G.F.	88	Y	···	52
	MM2	48.6625	−0.2972	None	···	Y	···	39
MSXDC G053.11+00.05								
	MM1	53.1406	0.0715	Red	981	Y	Y[e]	124
	MM2	53.1581	0.0641	G.F.	···	···	···	44
	MM3	53.0920	0.1200	Red	422	···	···	12
	MM4	53.1301	0.0517	G.F.	···	···	···	45
	MM5	53.1364	0.0281	Red	749	···	···	13
MSXDC G053.25+00.04								
	MM1	53.2603	0.0384	None	59	Y	···	24
	MM2	53.2387	0.0537	Blue	50	···	···	74
	MM3	53.2271	−0.0023	None	7	···	···	10
	MM4	53.2507	0.0547	G.F.	89	Y	···	12
	MM4	53.2522	0.0515	G.F.	···	Y	···	12
	MM5	53.2167	0.0128	None	8	Y	···	19
	MM6	53.2190	0.0517	G.F.	1301	Y	Y	17
MSXDC G053.31+00.00								
	MM1	53.3312	0.0275	None	6	···	···	31
	MM2	53.2991	0.0456	None	···	···	···	33
	MM3	53.3238	0.0248	None	9	Y	···	8

Notes.
[a]The position of the core, as determined by Rathborne et al. (2006). If the core contains a green fuzzy, the central position of the green fuzzy is listed.
[b]The mass of the cores calculated by Rathborne et al. (2006) using a dust temperature of 15 K and an emissivity index, β, of 2.
[c]Maser and thermal emission line.
[d]Extended 24 μm source.
[e]Thermal emission line only.

correlation of H_2O and CH_3OH maser detection with IRAC and 24 μm emission.

A previous VLA H_2O maser survey was carried out by Wang et al. (2006) toward 140 of these cores (the cold cores identified by Rathborne et al. (2006)) with a total of 17 H_2O masers detected. Because of our improved sensitivity (∼40 mJy, as opposed to ∼1 Jy limit for Wang et al. (2006)) and our larger source list, we detected ∼4 times as many maser sources as Wang et al. (2006).

In addition to CH_3OH masers, 10 thermal CH_3OH lines were detected toward the cores. These thermal CH_3OH lines are easily distinguished from the masers by their larger linewidths: $\Delta V > 3$ km s^{-1} for the thermal lines, whereas $\Delta V < 1$ km s^{-1} for the maser lines. Of the 10 cores with thermal CH_3OH emission,

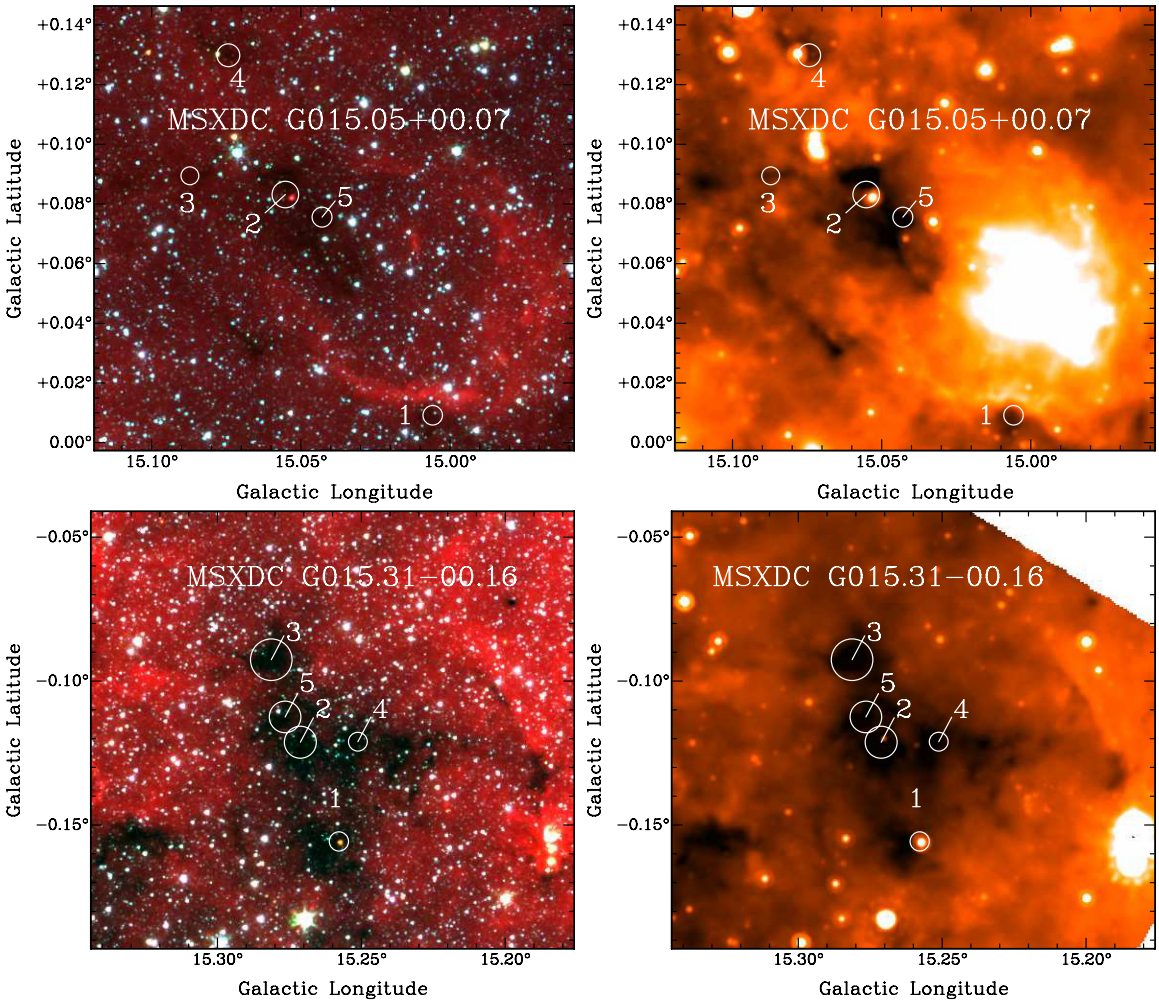

Figure 3. Left: IRAC 3-color (8.0 μm in red, 4.5 μm in green, 3.6 μm in blue) images of IRDCs. Right: *Spitzer*/MIPS 24 μm images of the same IRDCs. Each image is labeled with the name of the IRDC (from Simon et al. 2006a), and each core is labeled with its number designation (from Rathborne et al. 2006). Circles mark the position and angular size of each core. Boxes mark the positions of the green fuzzies.

four are active cores, three are intermediate cores, two are red cores, and one is a blue core.

4. DISCUSSION

Based solely on IR emission, we have separated the 190 cores into five specific classes–quiescent cores, intermediate cores, active cores, red cores, and blue cores. To be conservative, we exclude the intermediate cores from further analysis since they have only one of the two reliable IR star formation indicators. Because the blue cores are probably associated with foreground stars, we also exclude them from further analysis. We suggest that the remaining three classes, quiescent, active, and red, form an evolutionary sequence in the process of star formation.

4.1. Hypothetical Evolutionary Sequence for Cores within IRDCs

In this hypothetical sequence of the evolution of cores within IRDCs, the earliest stage is the quiescent core. Quiescent cores contain no green fuzzies, no 24 μm point sources, and no significant mid-IR IRAC emission. Because of the lack of these star formation indicators, quiescent cores may well be preprotostellar cores in an early evolutionary state, the cold precursors to star-forming cores. The lack of IR emission from quiescent cores is consistent with their detection as cold, dense cores with high column densities derived from (sub)mm continuum emission. The quiescent cores may be starless cores, many of which are high mass.

The active core phase woud then follow the quiescent core phase. Active cores contain both green fuzzies and 24 μm point sources. Because a green fuzzy indicates shocked gas, and a 24 μm point source reveals the heated dust around an embedded protostar, the detection of both of these IR signatures is strong evidence for embedded star formation.

Finally, the red cores are the last stage in this hypothetical evolutionary sequence for cores within IRDCs. Red cores are dominated by emission in the 8.0 μm band, which contains PAH features at 7.7 and 8.6 μm (Draine 2003). Because PAH emission is excited in regions with strong ultraviolet radiation fields, cores with PAH emission are likely in a later evolutionary state in which high-mass stars have already formed and begun to produce significant ultraviolet radiation. In addition, 94% of red cores are associated with 24 μm emission, indicative of a bright embedded protostar. Thus, the red cores probably contain

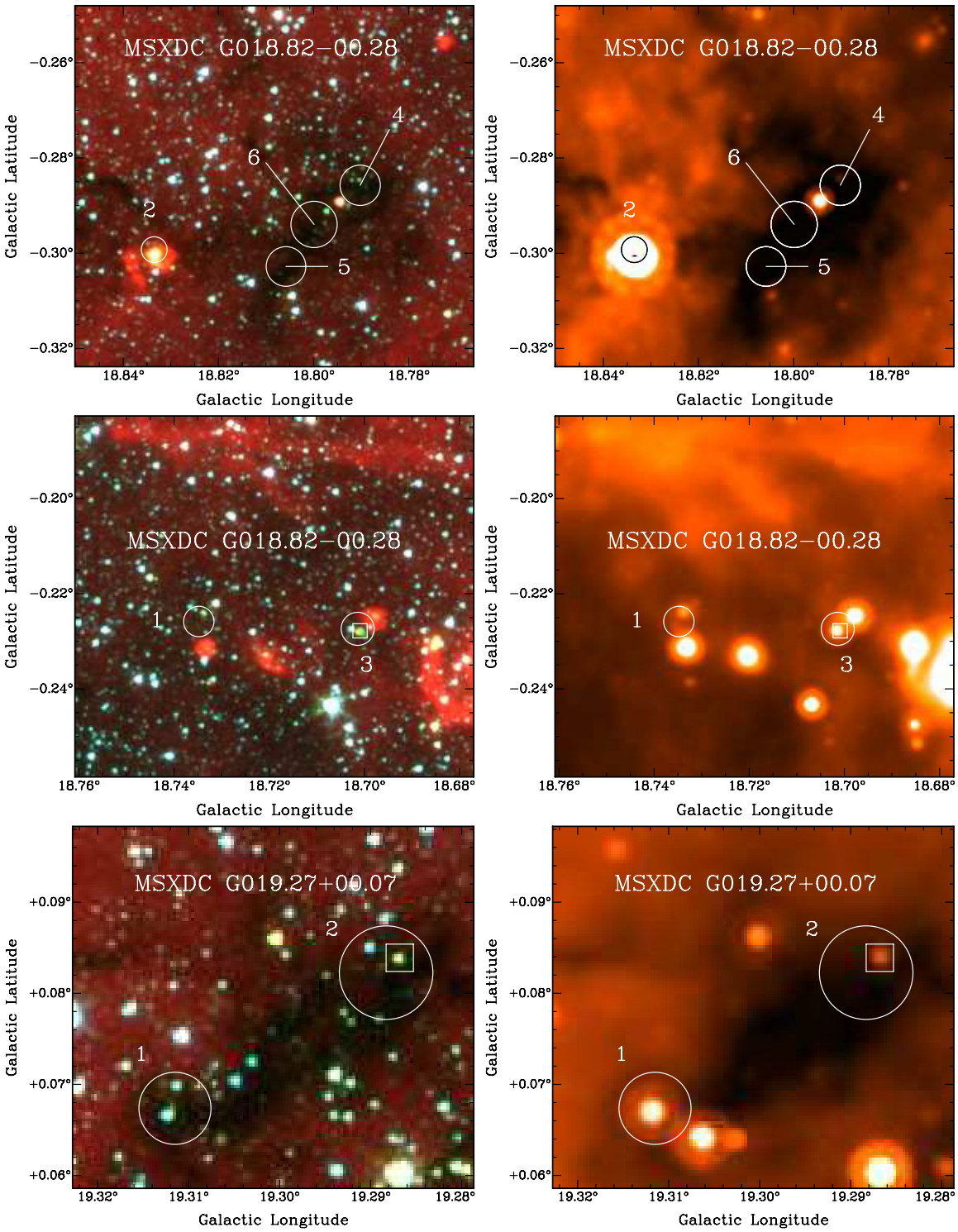

Figure 3. (Continued)

Hyper-Compact (HC) H II or Ultra-Compact (UC) H II regions. Only two red cores are unassociated with 24 μm emission. The MIPS detector is saturated for one of these cores, and the other core contains faint, diffuse 8 μm emission and no significant 24 μm emission.

To summarize, we suggest that the quiescent cores are in a preprotostellar state, the active cores are protostellar cores, and the red cores likely contain very young stars.

4.2. Relative Lifetimes

If we assume that we are sampling these cores at a random point in time, then the number of cores in a particular phase represents the amount of time spent in that phase. Thus, the fraction of cores in each phase is a rough measure of their relative lifetimes. If we consider only the preprotostellar (quiescent cores) and protostellar (active cores) phases, our sample contains 106 cores (69 quiescent and 37 active cores).

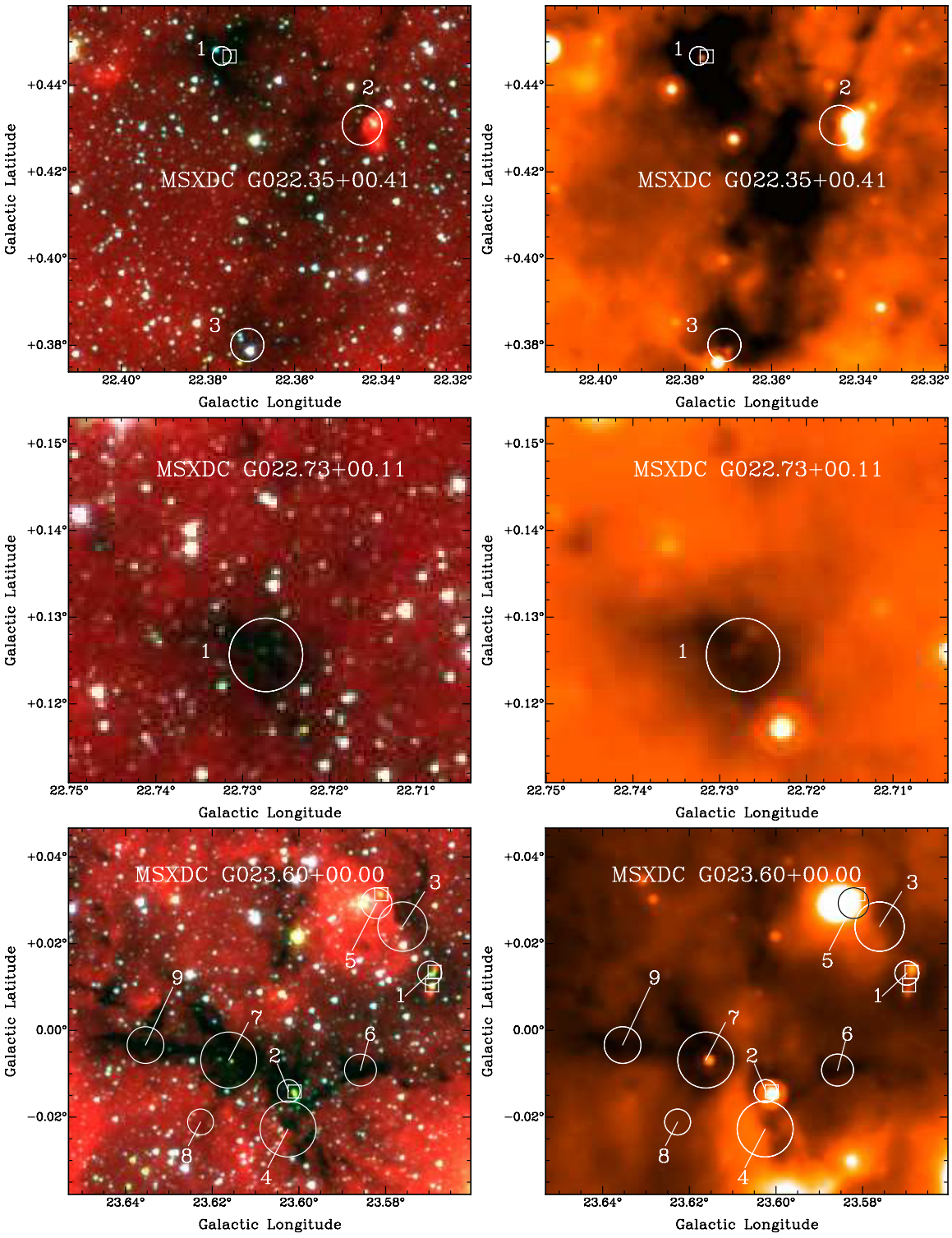

Figure 3. (Continued)

From our sample, we find that the first 65% of core evolution is spent in the quiescent phase, with no IR signatures of star formation. The last 35% of core evolution within IRDCs is spent in the active phase, with cores containing both a green fuzzy and a 24 μm point source. This phase ends with the formation of a HC/UC H II region (a red core).

We know that some cores within IRDCs are forming high-mass stars (e.g., Rathborne et al. 2005). If we assume that all cores within IRDCs will form high-mass stars, then we can begin to estimate the actual amount of time spent in the quiescent and active phases. The accretion timescale for high-mass star formation is not well determined, but is estimated to be anywhere from $\lesssim 10^5$ years up to $\sim 10^6$ years (e.g., Myers

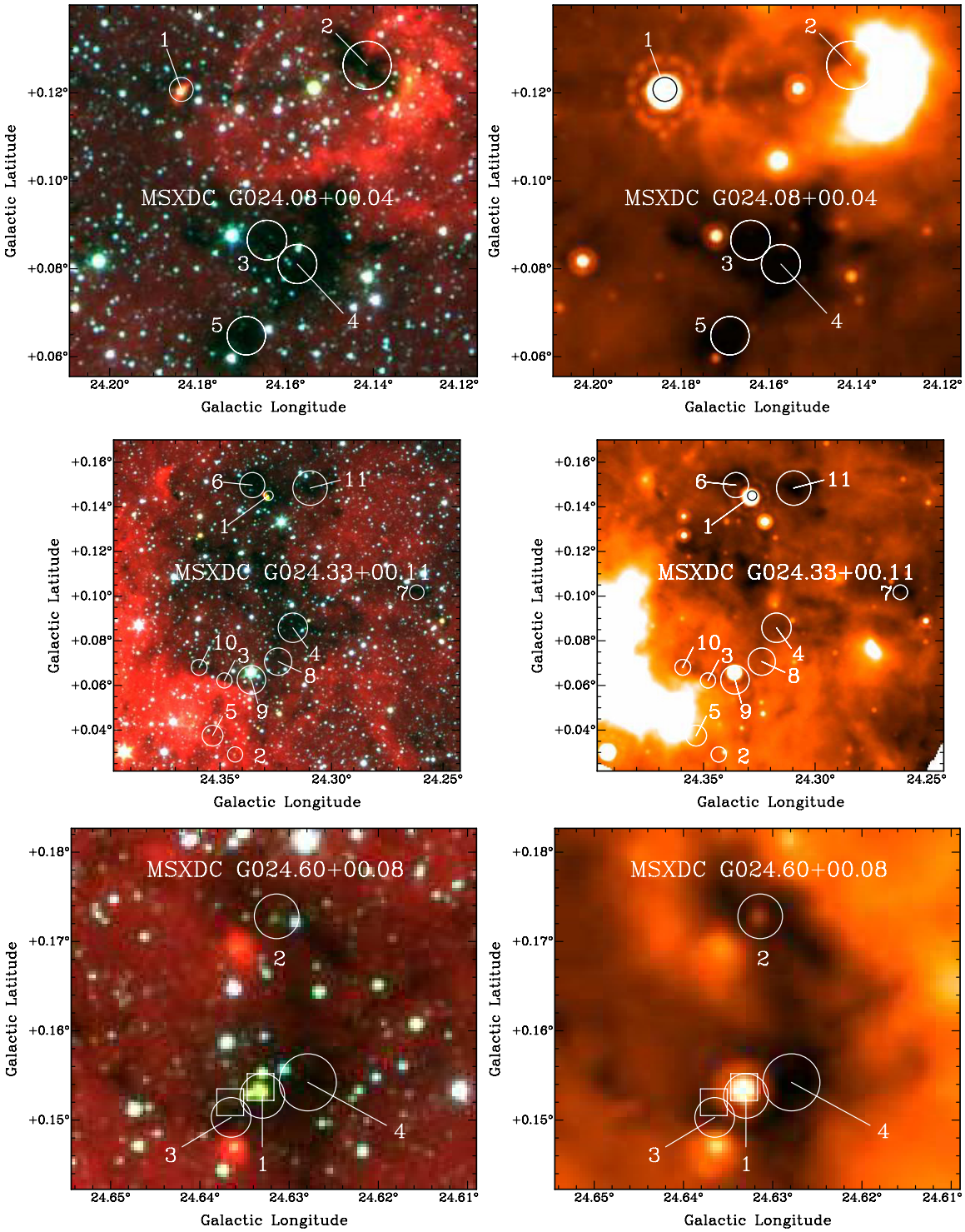

Figure 3. (Continued)

& Fuller 1992; Osorio et al. 1999; Behrend & Maeder 2001; McKee & Tan 2002; Zinnecker & Yorke 2007). We hypothesize that the accretion timescale is representative of the amount of time spent in the active core phase. Using the Zinnecker & Yorke (2007) accretion timescale of 200,000 years, we estimate that cores spend ∼370,000 years in the quiescent phase, followed by ∼200,000 years in the active phase.

These lifetime estimates are based on the assumption that we have detected all of the active and quiescent cores within the IRDCs. Because active cores likely have higher dust temperatures than quiescent cores, they are brighter emitters at mm wavelengths. As such, an active core of a given mass is easier to detect than a quiescent core of the same mass. Thus, if active and quiescent cores have similar mass distributions, there may be quiescent cores below our detection limit. Therefore, we may be underestimating the relative number of quiescent cores, and hence the amount of time spent in the quiescent core phase.

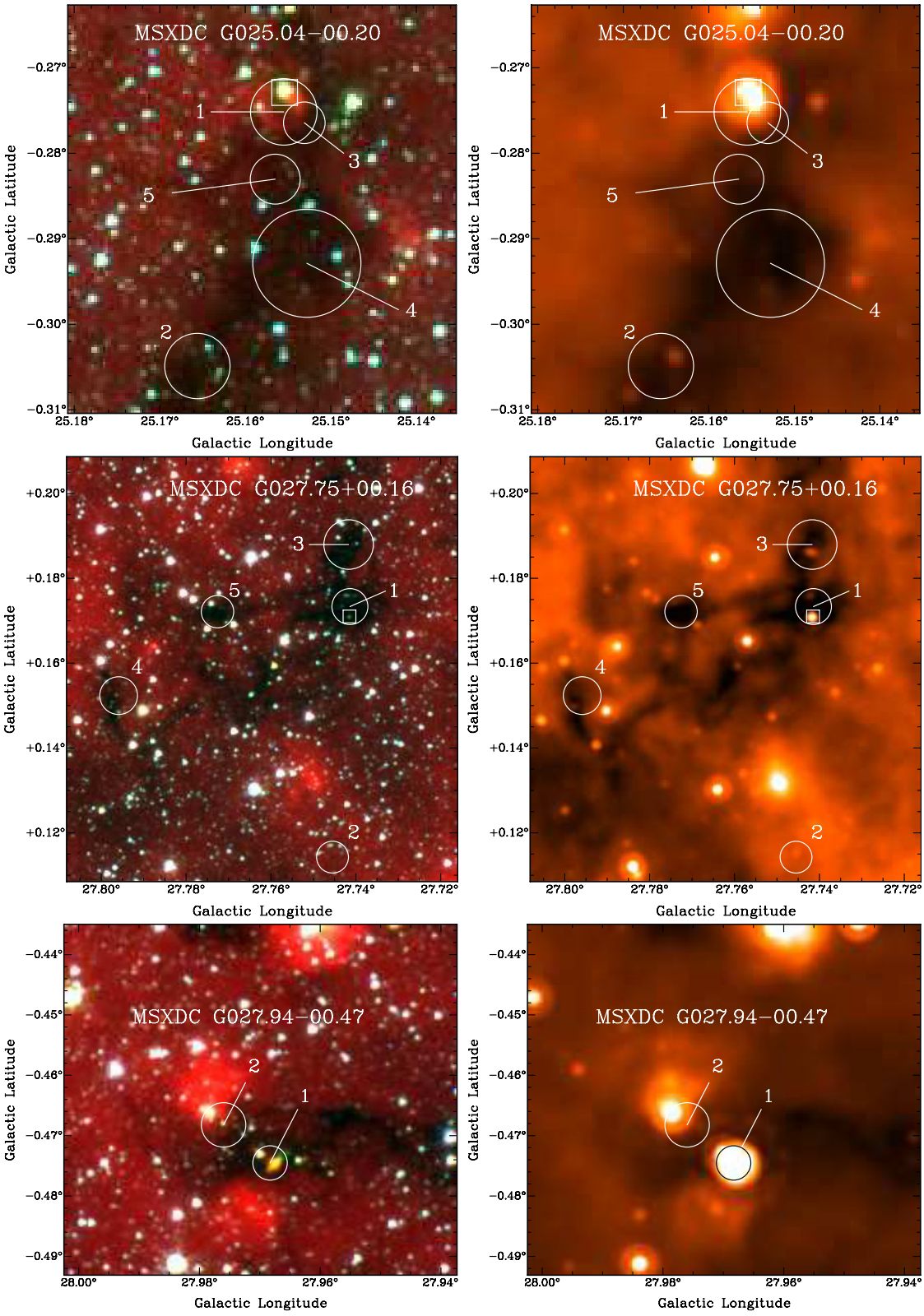

Figure 3. (Continued)

4.3. Sizes, Masses, and Densities of Active and Quiescent Cores

If active cores are indeed in a later evolutionary state than quiescent cores, then, because they have centrally condensed and formed protostars, active cores should be both smaller and denser than quiescent cores. To test this hypothesis, we examined both the physical sizes and densities of active and quiescent IRDC cores.

As expected, the physical sizes of the active cores are smaller than the quiescent cores (Figure 7). The cores' radii (FWHM of Gaussian fits to peaks in the 1.2 mm continuum emission)

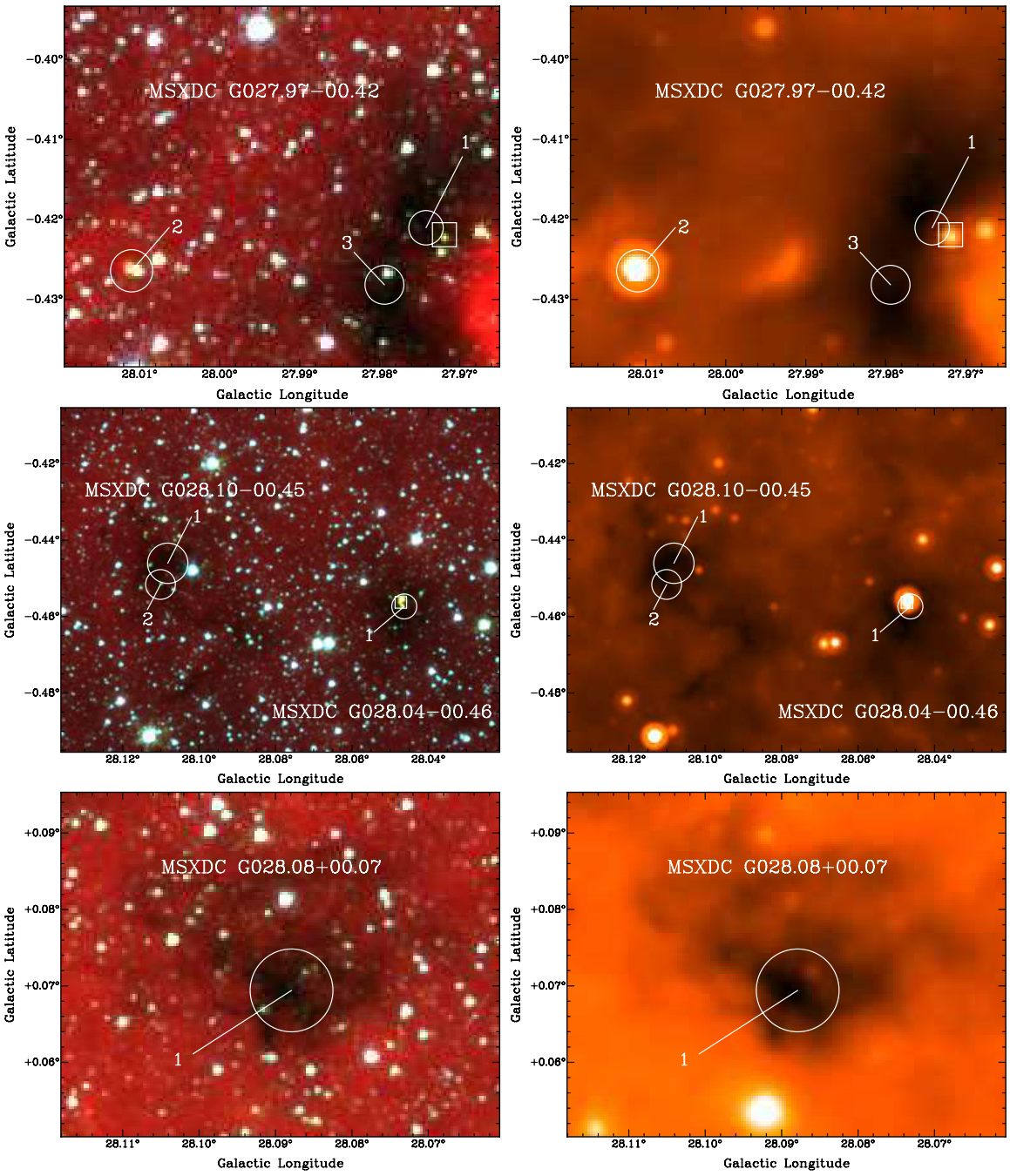

Figure 3. (Continued)

were determined by Rathborne et al. (2006) to range from 0.04 to 1.57 pc. The median size of the active cores (0.4 pc) is smaller than the median size of the quiescent cores (0.6 pc). The size distributions of active and quiescent cores are found to differ significantly by a Kolmogorov-Smirnov (K–S) test, which returns a probability of only 0.35% that they are part of the same underlying distribution. It is unclear whether the smaller size of active cores is due to gravitational collapse of the entire core or to the formation of a small, bright region in the core center. Because of the 11″ angular resolution of the 1.2 mm continuum data, we cannot distinguish between these two possibilities. Nevertheless, the smaller sizes of the active cores indicate that the active cores are distinct from quiescent cores.

In addition to the difference in the physical sizes between active and quiescent cores, Figure 8 shows that active cores also tend to be more massive (median mass of 233 $M_{\odot}$) than quiescent cores (median mass of 118 $M_{\odot}$). We consider three possible explanations for this difference in mass distributions.

First, the difference may suggest that more massive cores evolve on a shorter timescales than lower mass cores, and thus high-mass cores may spend a larger fraction of their lifetimes in the active phase.

Second, our designations of active and quiescent cores could be a selection effect active cores may simply be more luminous, higher-mass versions of the lower mass quiescent cores. In this case, the active cores would represent cores in which luminous

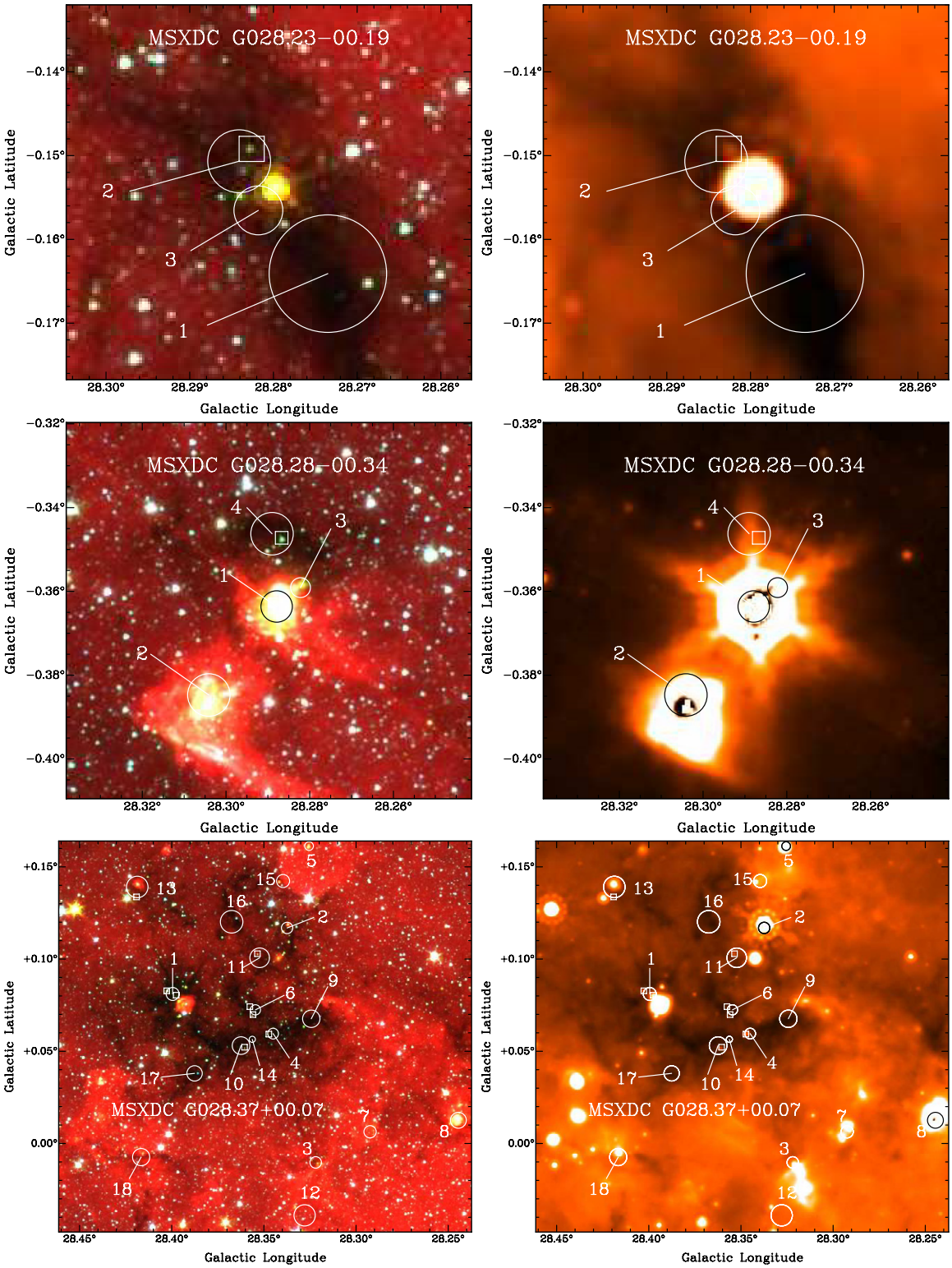

Figure 3. (Continued)

high-mass stars are forming, but the quiescent cores would represent cores in which only faint low-mass stars are forming. If this is the case, then quiescent cores may not evolve into what we identify as active cores.

Third, the apparent difference in masses may simply arise from a temperature effect. The masses of the cores were calculated by Rathborne et al. (2006) assuming a dust temperature of 15 K and an emissivity index, β, of 2 for every core. However, if active cores contain luminous protostars, their dust temperatures are probably warmer than 15 K. Because the derived mass decreases with increasing temperature, the mass calculated with a dust temperature of 15 K will overestimate the

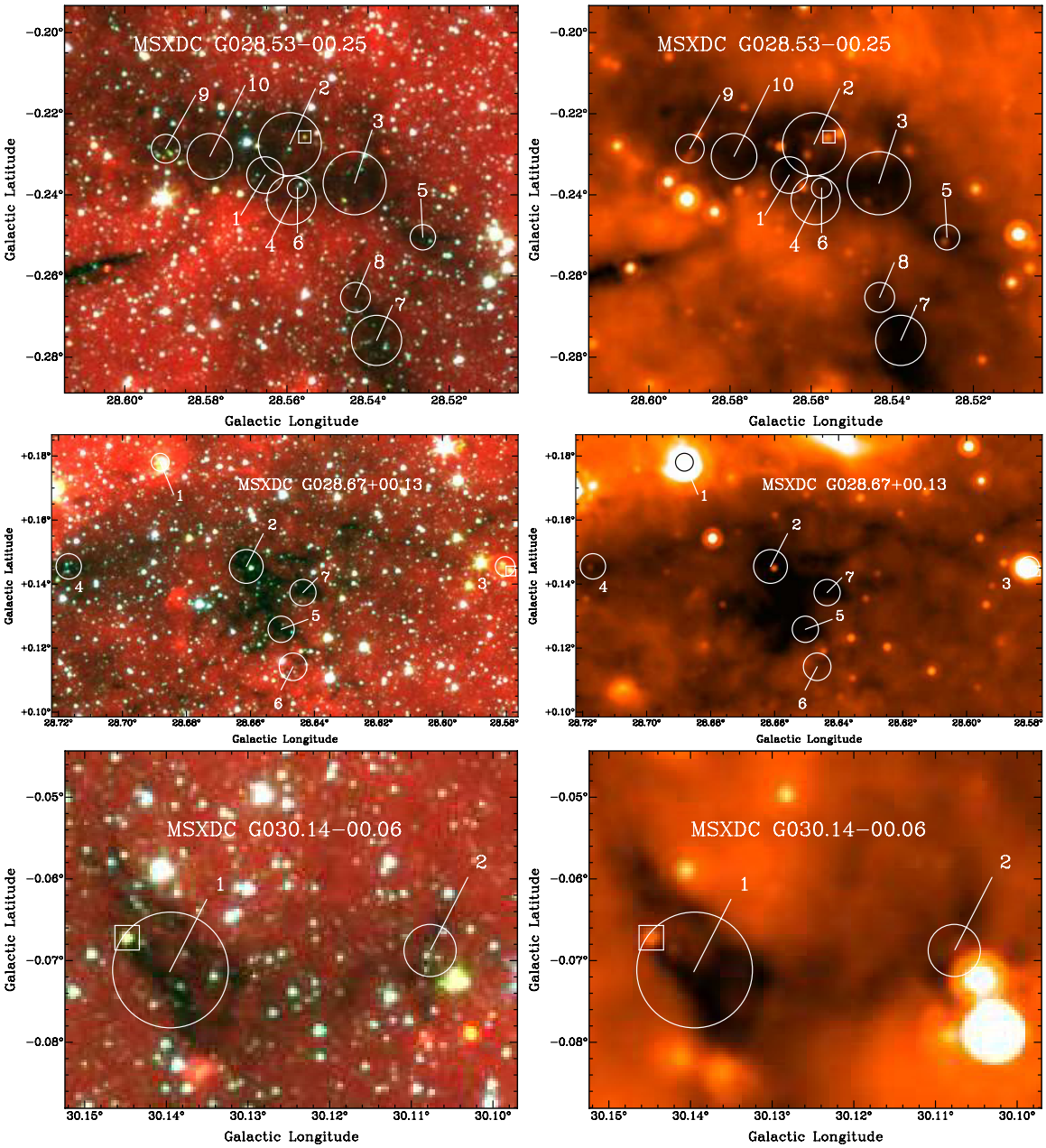

Figure 3. (Continued)

actual mass of the warmer active cores. If we assume that the mass distribution of active and quiescent cores is the same, then we can find a new temperature for the mass calculation of active cores which aligns the active and quiescent mass distributions. We find that a dust temperature of 25 K (to the nearest 5 K) maximizes the likelihood (77.2% using the K–S test) that active and quiescent cores have the same mass distribution.

If active cores are condensing from the earlier quiescent core state to form stars, then active cores should also be denser than quiescent cores. Using the masses and sizes of the cores, we calculate and compare the $n(H_2)$ distributions of active and quiescent cores. The active cores are indeed denser (the mean density of the active cores is 6.9×10^4 cm^{-3} and the mean density of the quiescent cores is 2.3×10^4 cm^{-3}; see Figure 9). However, as described above, we may be overestimating the masses of active cores due to the assumption of a uniform dust temperature of 15 K. The density distribution of active and quiescent cores may, therefore, simply reflect this mass overestimate. Using the masses derived with a new dust temperature of 25 K for the active cores (see above), we recalculate the density distribution of the active cores and compare it to the density distribution of quiescent cores. Even with the lower masses for the active cores, the active cores (mean density of 3.5×10^4 cm^{-3}) are still denser than quiescent cores (mean density 2.3×10^4 cm^{-3}; see Figure 9).

In addition to the volume density, we can also examine the surface mass density, Σ, of the active and quiescent cores. According to Krumholz & McKee (2008), the minimum surface mass density required for high-mass star formation, $\Sigma_{\rm th}$, is 1 g cm^{-2}. We calculate the peak surface mass density for active and quiescent cores using the peak 1.2 mm flux of each core

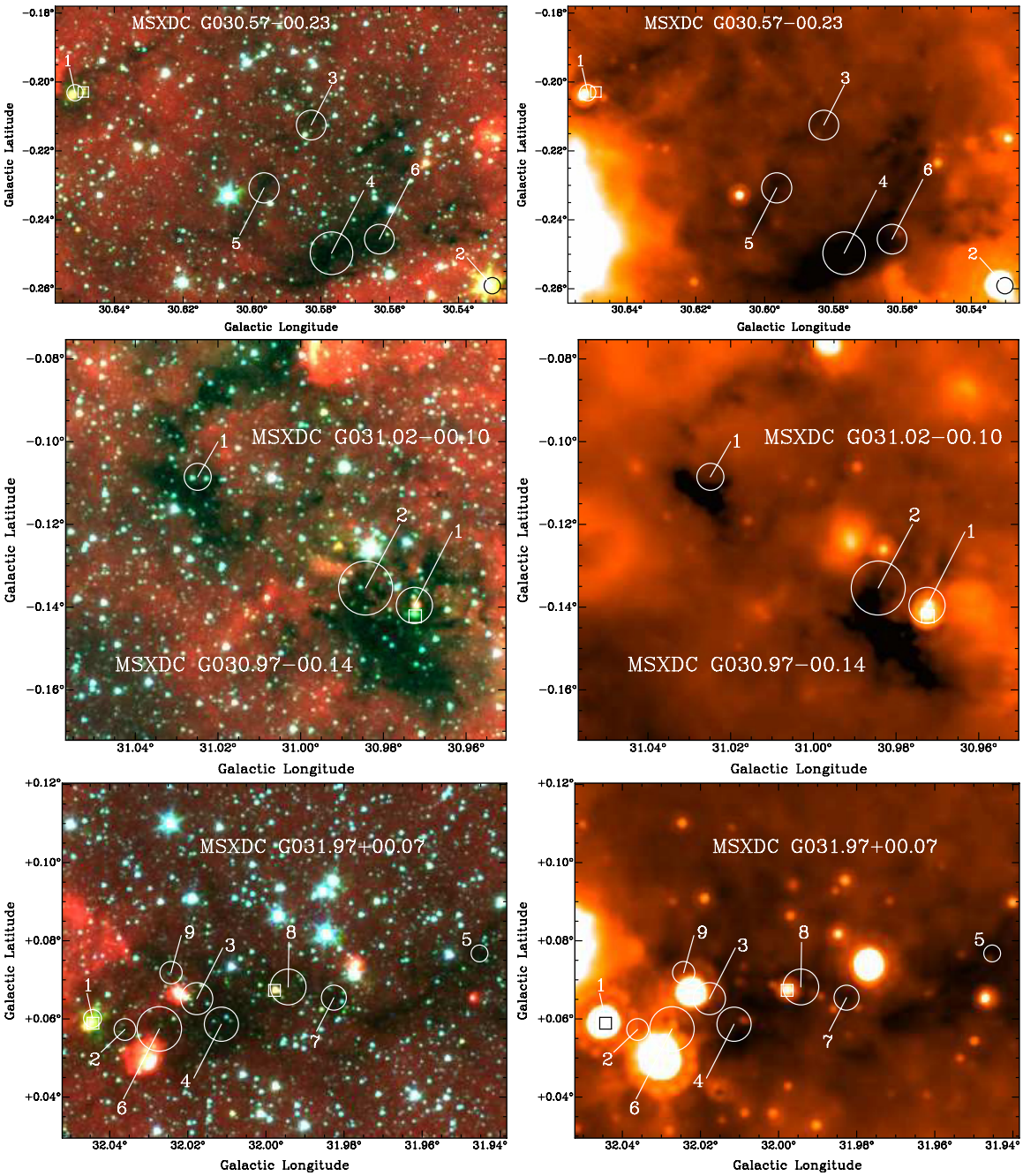

Figure 3. (Continued)

(from Table 3 in Rathborne et al. 2006) to estimate the mass (assuming a dust temperature of 15 K), and the angular size of the IRAM 30m beam (11.″5 for 1.2 mm observations) to estimate the surface area of each core. For quiescent cores, we find a median surface mass density of 0.26 g cm^{-2}, with two cores (∼3%) above $\Sigma_{\rm th}$, and for active cores, we find a median surface mass density of 0.45 g cm^{-2}, with 11 cores (∼30%) above $\Sigma_{\rm th}$ (Figure 10). Because active cores may be warmer than 15 K due to embedded protostars, we recalculate Σ for the active cores using a dust temperature of 25 K. With this higher temperature for active cores, we find a median surface mass density of 0.23 g cm^{-2}, with three cores (∼14%) above $\Sigma_{\rm th}$ (Figure 10). While $\Sigma > \Sigma_{\rm th}$ for a small fraction of cores, the median Σ values for active and quiescent cores are both lower than 1 g cm^{-2}. It is possible that the surface mass density is being calculated over too large an area, resulting in decreased values of Σ, and that future interferometric studies of Σ in protostellar condensations within these cores may result in Σ values closer to $\Sigma_{\rm th}$. Alternatively, the size scales used to calculate Σ may be correct, and the detection of high-mass protostars (Rathborne et al. 2006) within some active cores where $\Sigma < \Sigma_{\rm th}$ suggests that the theoretical expectation that $\Sigma_{\rm th} = 1$ g cm^{-2} may be in error. The similarity of median Σ values for active (0.23 g cm^{-2}, assuming a dust temperature of 25 K) and quiescent cores (0.26 g cm^{-2}, assuming a dust temperature of 15 K) indicates that the separation of cores within IRDCs into active and quiescent cores is probably not the result of a surface mass density selection effect.

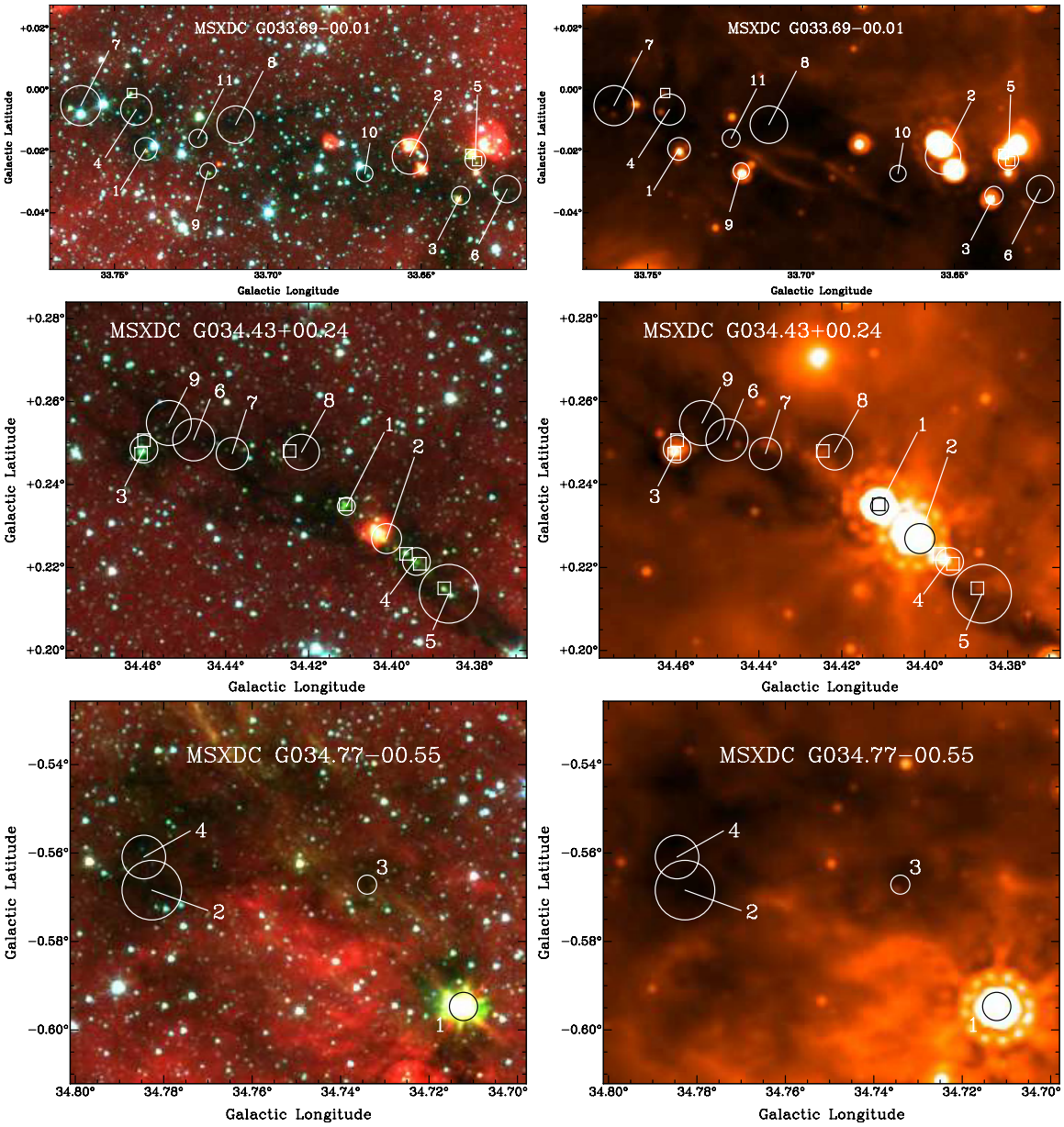

Figure 3. (Continued)

4.4. Masers as a Tracer of Star Formation

Both H_2O and CH_3OH masers indicate star formation. Here, we use the results of our H_2O and CH_3OH maser survey to test our IR classifications of star formation activity in cores within IRDCs.

4.4.1. H_2O Masers

Because H_2O masers are a well-known signpost of star formation for both low-mass and high-mass stars, they can be used to indicate star formation activity within these cores. If our IR classification of quiescent, active, and red cores accurately reflects their star formation activity, then the percentage of cores containing H_2O masers should be significantly higher for active and red cores than for quiescent cores. As Table 5 shows, about 59% of active cores and 54% of red cores contain water masers, while only 16% of quiescent cores harbor water masers. Together, these percentages clearly demonstrate that star formation activity is indeed enhanced in the active and red cores. This result supports the idea that red and active cores are indeed a later, star-forming evolutionary state than quiescent cores. The detection of H_2O masers toward some quiescent cores suggests that a small fraction of the quiescent cores may be forming low-mass stars with undetected IR signatures.

The lack of H_2O maser detection toward 41% of active cores does not necesssarily mean that star formation within those cores is absent. Because maser emission is sensitive to viewing geometry, variable, or possibly fainter than our detection limit, many masers could have escaped detection. It is also possible that these cores have yet to enter or have already passed through the maser phase. Despite the non-detections toward active cores, however, a much higher percentage of masers was detected toward active cores than quiescent cores.

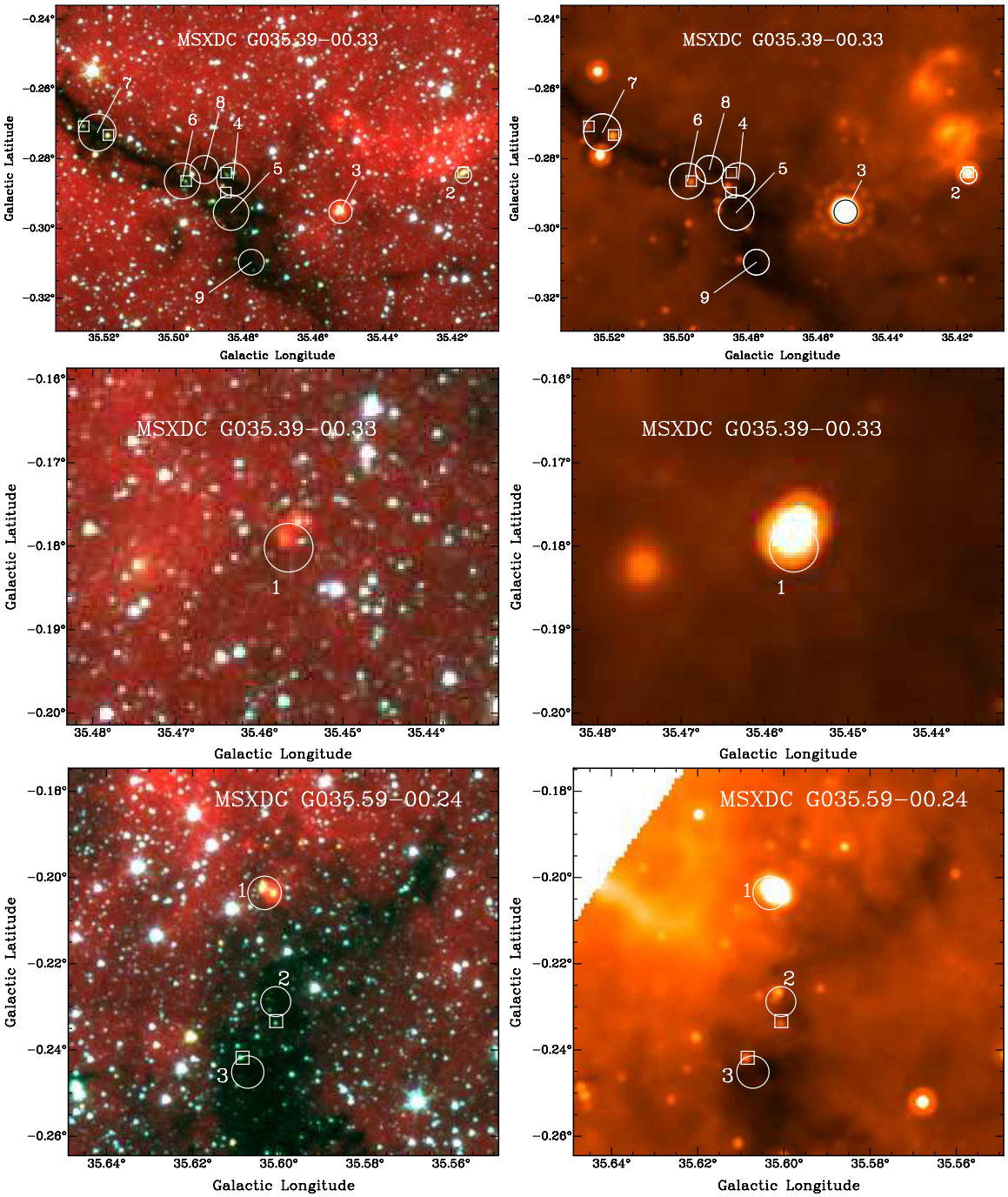

Figure 3. (Continued)

About half (34 of 67) of all H_2O maser spectra toward the detected cores show multiple velocity components (Figure 5). These multiple components may arise from different maser spots (along outflows, or in a disk) associated with a single protostar. Alternatively, they could be associated with multiple protostars within a single core. Future VLA maser studies may reveal the locations of the maser spots within the cores, allowing us to test the idea that each H_2O maser velocity component is associated with an individual protostar, and that some cores are forming clusters. Indeed, high angular resolution (sub)mm imaging of cores within IRDCs (Rathborne et al. 2007; Rathborne et al. 2008) shows that at least some active cores do contain multiple condensations, indicative of cluster formation.

4.4.2. CH_3OH Masers

CH_3OH masers are a well-known tracer of star formation. While the radiatively excited Class II CH_3OH masers are believed to trace only high-mass star formation (e.g., Walsh et al. 2001; Minier et al. 2003), the case is less clear for the collisionally excited Class I CH_3OH transitions. Until recently, Class I methanol masers were also thought to trace high-mass star formation exclusively, but the recent study of Kalenskiĭ

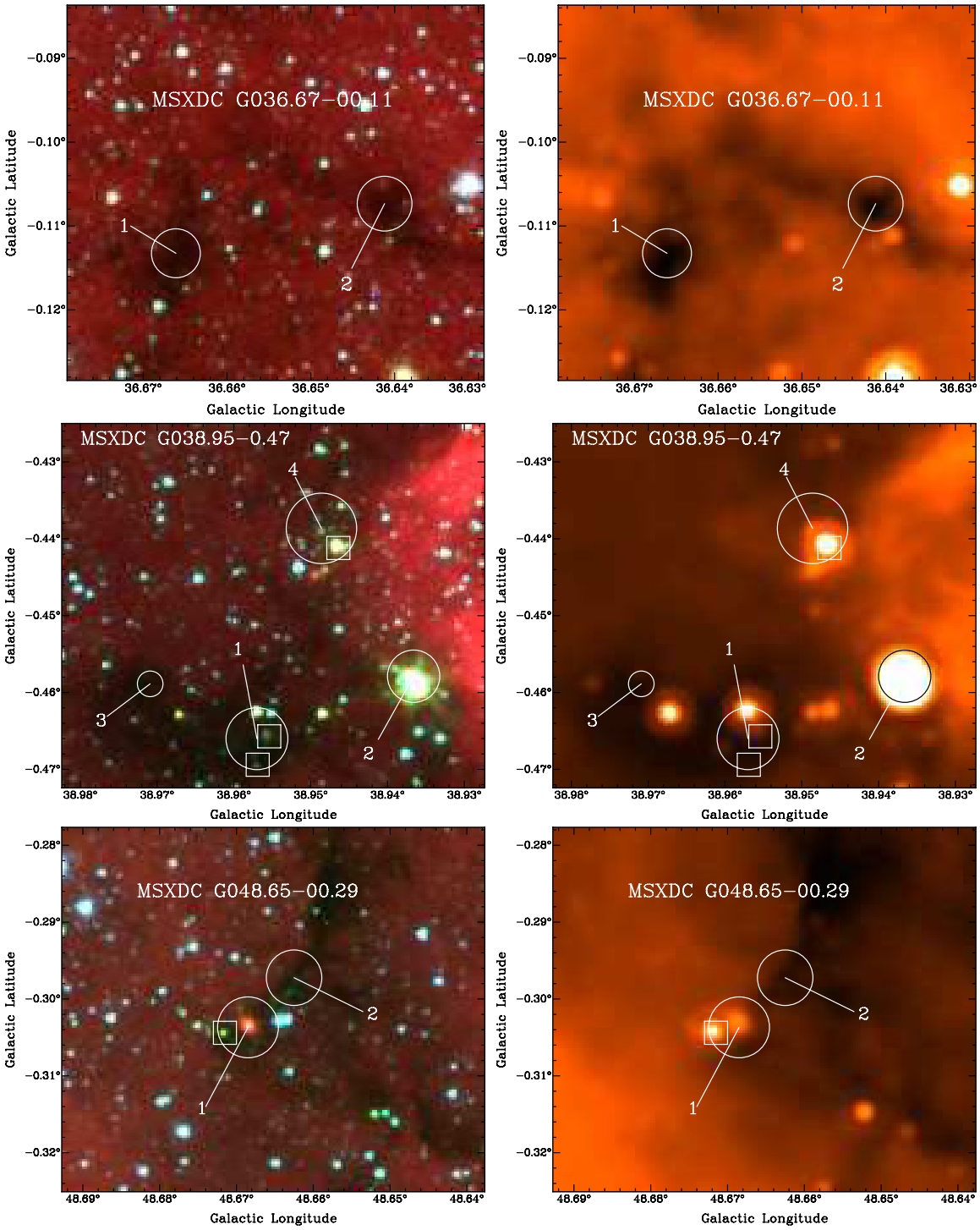

Figure 3. (Continued)

et al. (2006) shows that Class I CH_3OH masers may also be found toward low-mass star-forming regions. Thus, our detection of Class I CH_3OH masers toward 15 cores does not, on its own, mean that the cores are forming high-mass stars, but it does unambiguously indicate star-formation activity.

Almost all (93%) cores with CH_3OH masers also contain H_2O masers. This could be a function of evolutionary state, and perhaps all cores with H_2O masers will eventually produce CH_3OH masers. Another possibility is that Class I CH_3OH maser emission does preferentially trace high-mass star formation, and only the high-mass star-forming cores will have both CH_3OH and H_2O masers. The small number of CH_3OH masers (compared to the larger number of H_2O masers), suggests that the CH_3OH maser lifetime is much shorter than the H_2O maser lifetime.

4.4.3. Masses of Cores with Masers

The mass distribution of cores associated with both H_2O and CH_3OH maser detections shows that masers are preferentially

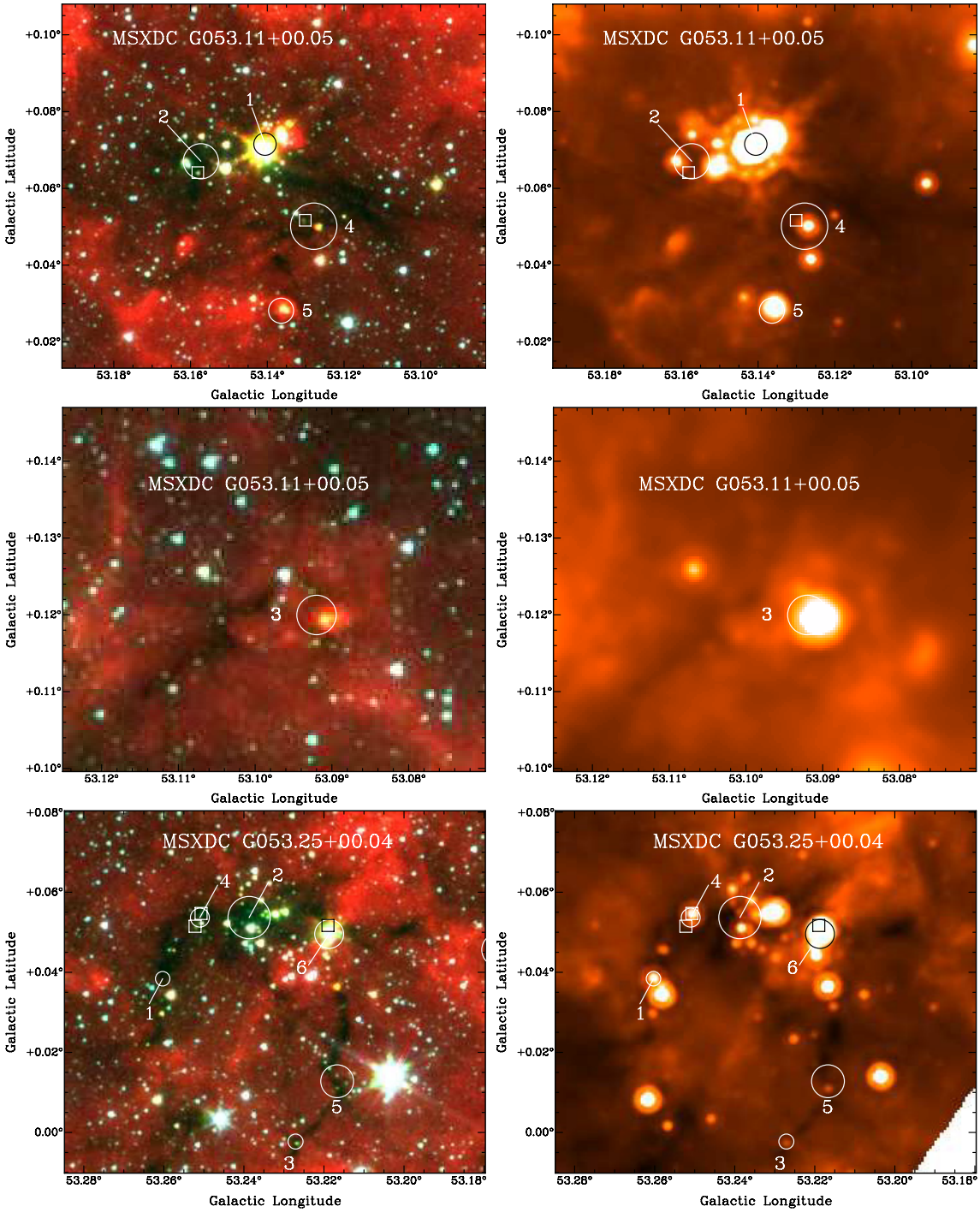

Figure 3. (Continued)

detected toward higher mass cores (Figure 11). K–S tests of the distributions of core masses with and without masers show probabilities of 0.2% and 1.1% for H_2O and CH_3OH, respectively, that the mass distributions of cores with and without masers are drawn from the same parent distribution. If core mass correlates with final stellar mass (Alves et al. 2007), then the tendency of high-mass cores to harbor masers would suggest that masers may be preferentially tracing cores that are forming high-mass ($M \geqslant 8\ M_{\odot}$) stars.

The apparent correlation of maser activity with core mass might also reflect a temperature bias. As discussed in Section 4.3, active cores are probably warmer than quiescent cores, and if so, the masses based on mm continuum measurements (Rathborne et al. 2006) under the assumption of a common dust temperature of 15 K are overestimated. To test the possibility of a temperature bias, we again assign a dust temperature of 25 K to the active cores, thereby reducing their derived masses. With the new mass distribution of maser detections, a repeat of the K–S test of cores with and without H_2O and CH_3OH masers returns higher probabilities (11.47% and 11.01%, respectively) that the cores with and without masers are part of the same underlying distribution. Even though these probabilities are higher, it still

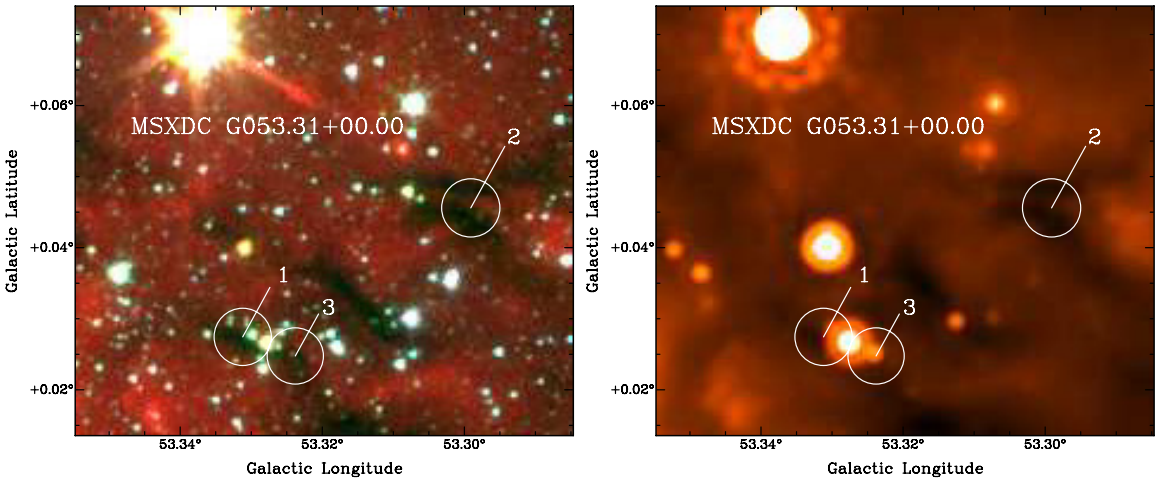

Figure 3. (Continued)

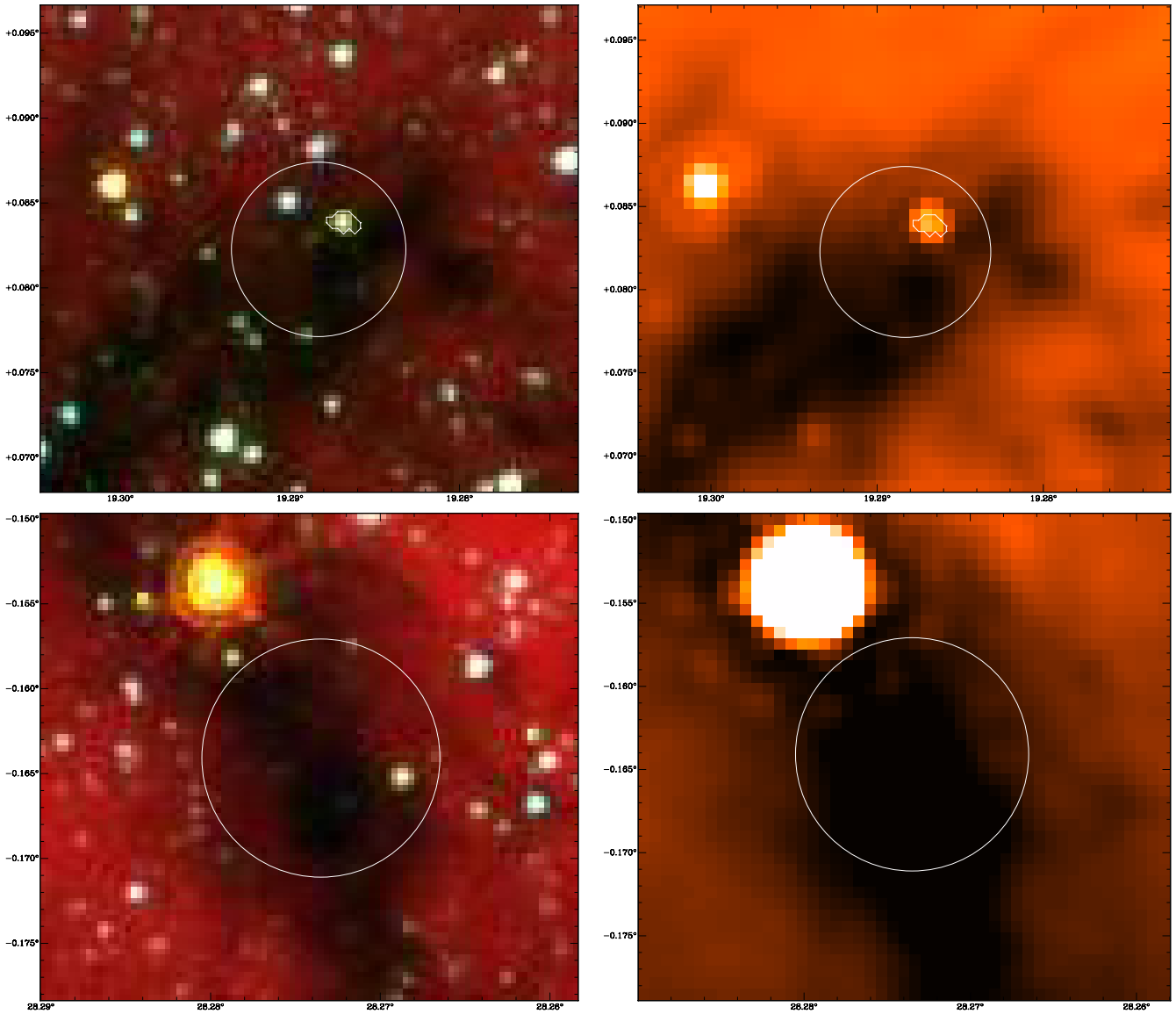

Figure 4. GLIMSPE 3-color (8.0 μm in red, 4.5 μm in green, 3.6 μm in blue) and 24 μm images of an active core (top) and a quiescent core (bottom). The circles mark the position and angular size of the cores. The active core contains a green fuzzy (white contour), while the quiescent core contains no significant IRAC emission. The active core contains a 24 um point source, while the quiescent core does not.

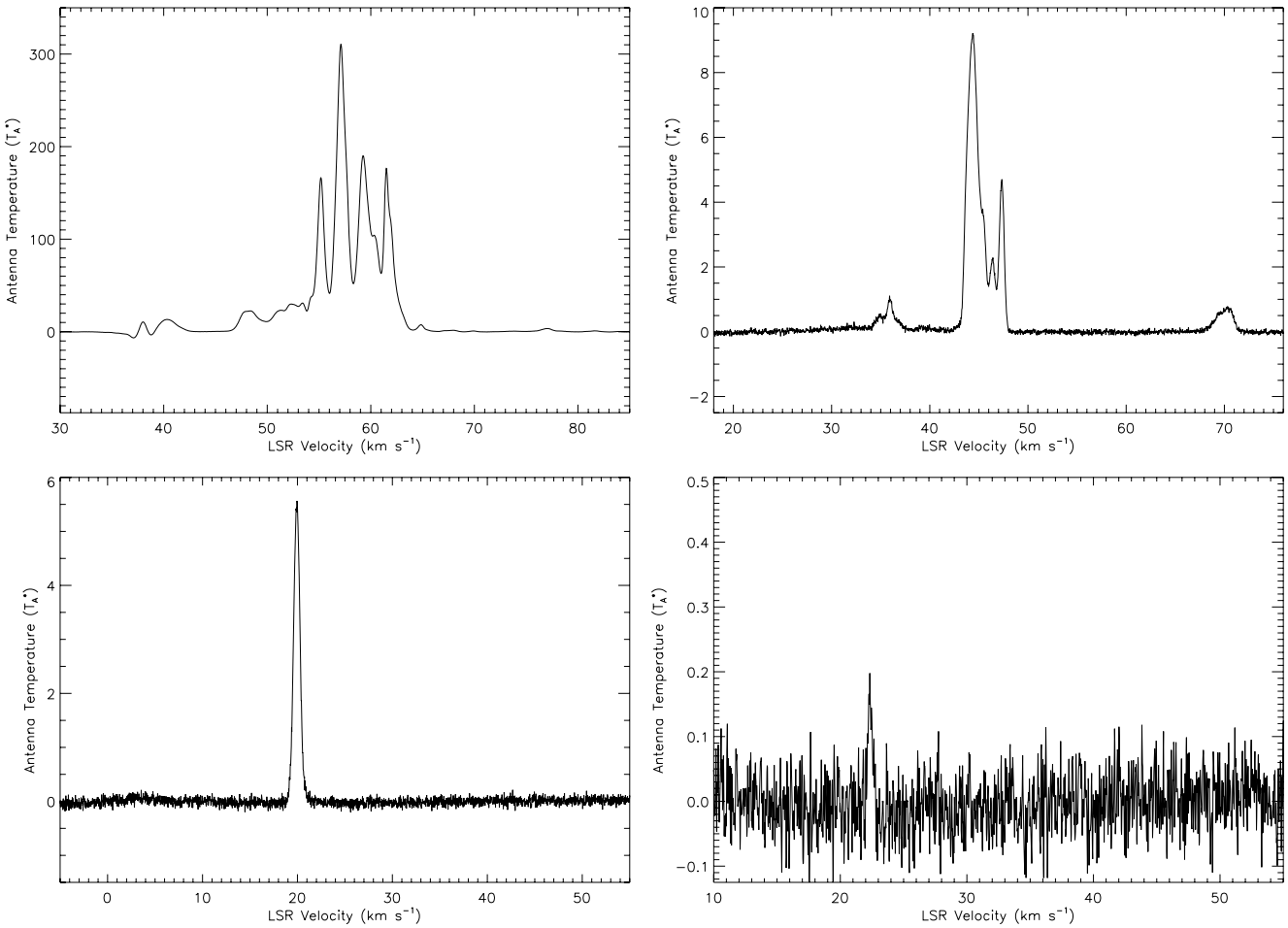

Figure 5. H_2O maser spectra taken with the GBT toward four cores. Top: two cores (left: MSXDC G034.43+00.24 MM1 and right: MSXDC G027.94−00.47 MM1) which have spectra with multiple velocity components. Thirty four of 67 water maser spectra show multiple velocity components. Bottom: two cores (left: MSXDC G053.25+00.04 MM4 and right: MSXDC G053.25+00.04 MM5, Hanning smoothed) have a single-velocity component. Thirty three of 67 water maser spectra show a single velocity component.

Table 3
Summary of Results

	Number	Green Fuzzy	Red	Blue	No IRAC	24 μm Source	H_2O Maser	CH_3OH Maser
Green Fuzzy	47 (57[a])	...	...	...	...	74%	51%	17%
Red	35	...	...	...	...	77%	54%	11%
Blue	6	...	...	...	...	67%	17%	17%
No IRAC	102	...	...	...	...	29%	23%	2%
24 μm Source	98 (103[a])	41%	28%	4%	31%	...	50%	12%
H_2O Maser	67	36%	28%	1%	34%	73%	...	21%
CH_3OH Maser	15	53%	27%	7%	13%	80%	93%	...

Notes. [a]47 cores contain a total of 57 individual green fuzzies (10 cores contain two green fuzzies). 98 cores contain a total of 103 individual 24 μm point sources (five cores contain two 24 μm point sources; we search for a 24 μm point source toward each green fuzzy). The correlation between green fuzzies and 24 μm point sources is the only calculations which use the number of individual sources; all other calculations are based on the number of cores.

Table 4
Core Classification Summary

IRAC Characterization	24 μm Emission	Core Classification
Bright 8.0 μm emission	Yes or No	Red Core
Green Fuzzy	Yes[a]	Active Core
Green Fuzzy	No	Intermediate Core
None	Yes	Intermediate Core
None	No	Quiescent Core
Bright 3.6 μm emission	Yes or No	Blue Core

Notes. [a]Includes only point source emission.

remains likely (∼90% confidence) that cores with H_2O and CH_3OH masers have higher masses than cores with no masers.

4.4.4. Cores with Thermal CH_3OH Emission

Thermal CH_3OH emission is indicative of a rich chemical environment, perhaps arising from a hot core (or corino). Because the hot core stage occurs when a protostar has formed, we would only expect those cores in the later stages of our hypothetical evolutionary sequence to display thermal CH_3OH emission. Indeed, none of the thermal lines were detected toward quiescent cores.

4.5. High-Mass Starless Core Candidates

A direct result of our classification scheme is a list of starless core candidates–the quiescent cores. If we assume that each quiescent core will form only one star with a 30% star formation efficiency (e.g., Alves et al. 2007; Enoch et al. 2008), then the

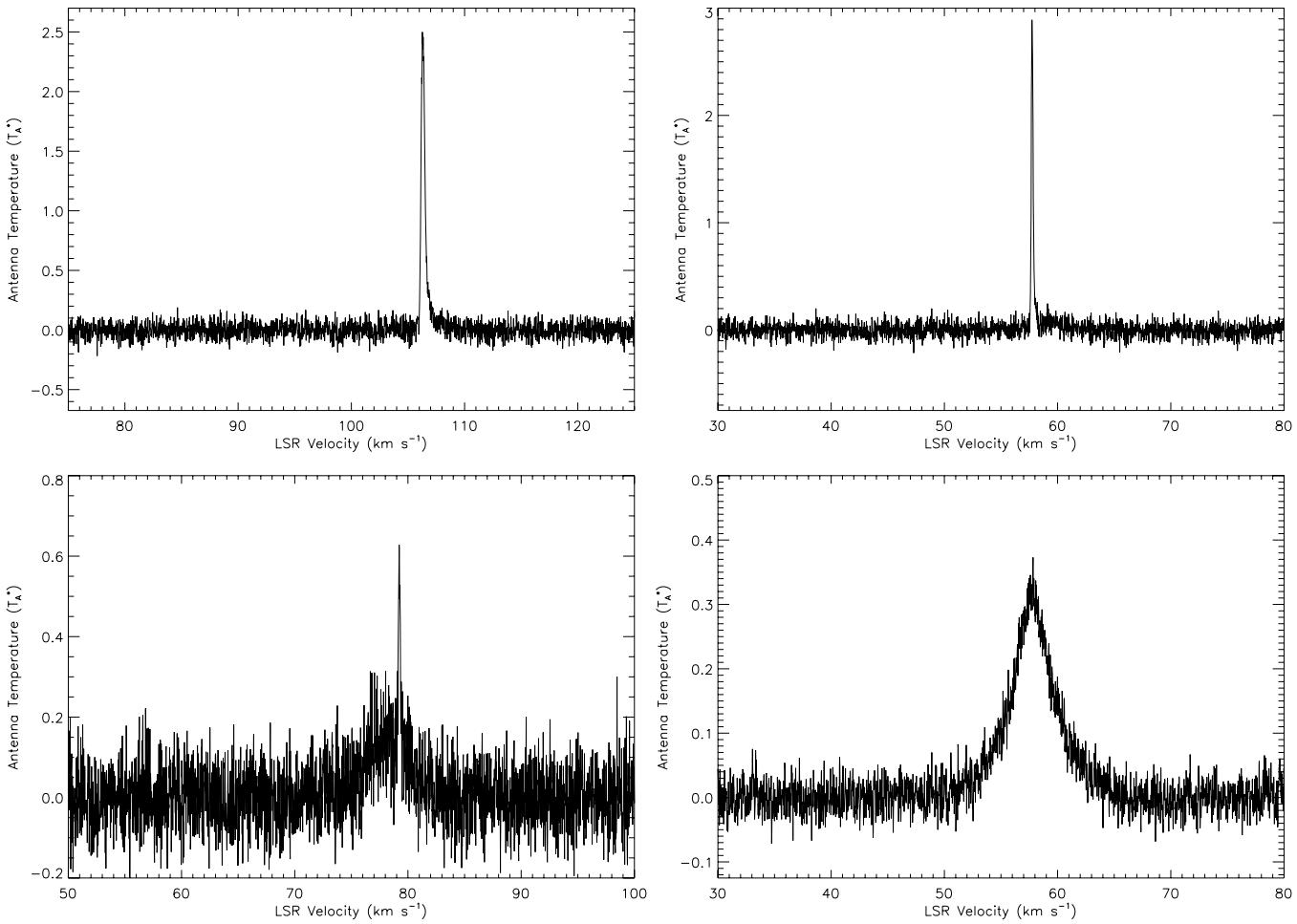

Figure 6. CH_3OH spectra taken with the GBT toward four cores. Top: two cores (left: MSXDC G023.60+00.00 MM1 and right: MSXDC G034.43+00.24 MM3) which only show maser emission. Bottom-left: a core with both thermal CH_3OH emission and CH_3OH maser emission (MSXDC G028.37+00.07 MM1). Bottom-right: a core which only shows thermal CH_3OH emission (MSXDC G034.43+00.24 MM1).

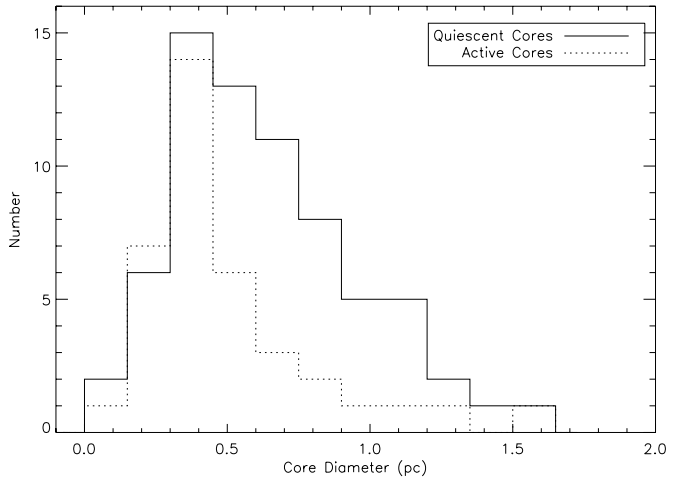

Figure 7. Core diameter histograms of active (dotted line) and quiescent (solid line) cores. Active cores are smaller than quiescent cores, as expected if active cores are collapsing to form stars. According to the results of a K–S test, there is only a 0.35% probability that these two samples are part of the same underlying distribution.

lower mass limit for a core which can produce a high-mass ($M \geqslant 8\ M_\odot$) star is $\sim$25 $M_\odot$. Applying this mass limit to our list of quiescent cores results in a total of 65 high-mass starless core candidates. Alternatively, we can assume that each core will form multiple stars with a mass distribution determined by the IMF. According to the Miller & Scalo (1979) IMF, $\sim$10% of the final *stellar* mass will be in high-mass stars. Coupling this percentage with a 30% star formation efficiency for each molecular protostellar condensation within the core yields a net high-mass star formation efficiency of about 3% for the entire prestellar core. Thus, any quiescent core with a mass $\gtrsim$ 270 $M_\odot$ could potentially form a high-mass star. Our sample contains 19 such cores. Using either assumption results in a significant number ($\gtrsim$ 20) of high-mass starless core candidates. Future studies of these candidate high-mass prestellar cores can help constrain the initial conditions for high-mass star formation.

Table 5
Summary of Maser Survey Detections

	Number	H_2O Maser	CH_3OH Maser
Red Cores	35	19 (54%)	5 (14%)
Active Cores	37	22 (59%)	5 (14%)
Intermediate Cores	43	14 (33%)	4 (9%)
Quiescent Cores	69	11 (16%)	0 (0%)
Blue Cores	6	1 (17%)	1 (17%)

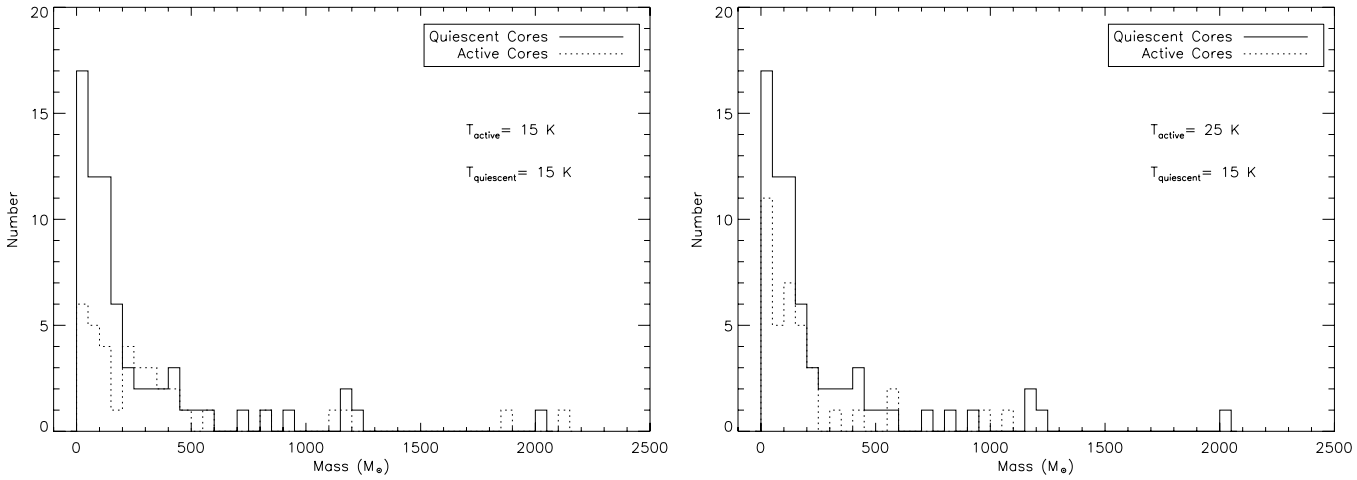

Figure 8. Mass histograms of active (dotted line) and quiescent (solid line) cores. Left: all core masses were calculated using a dust temperature of 15 K. Active cores (median mass of 233 $M_\odot$) are more massive than quiescent cores (median mass of 118 $M_\odot$). The masses of active cores will be overestimated, therefore, if active cores are warmer than quiescent cores. Right: the masses of the quiescent cores are calculated using a dust temperature of 15 K, while the masses of the active cores are calculated using a dust temperature of 25 K. The active core dust temperature of 25 K maximizes the likelihood (77.2% using the K–S test) that active and quiescent cores have the same mass distribution.

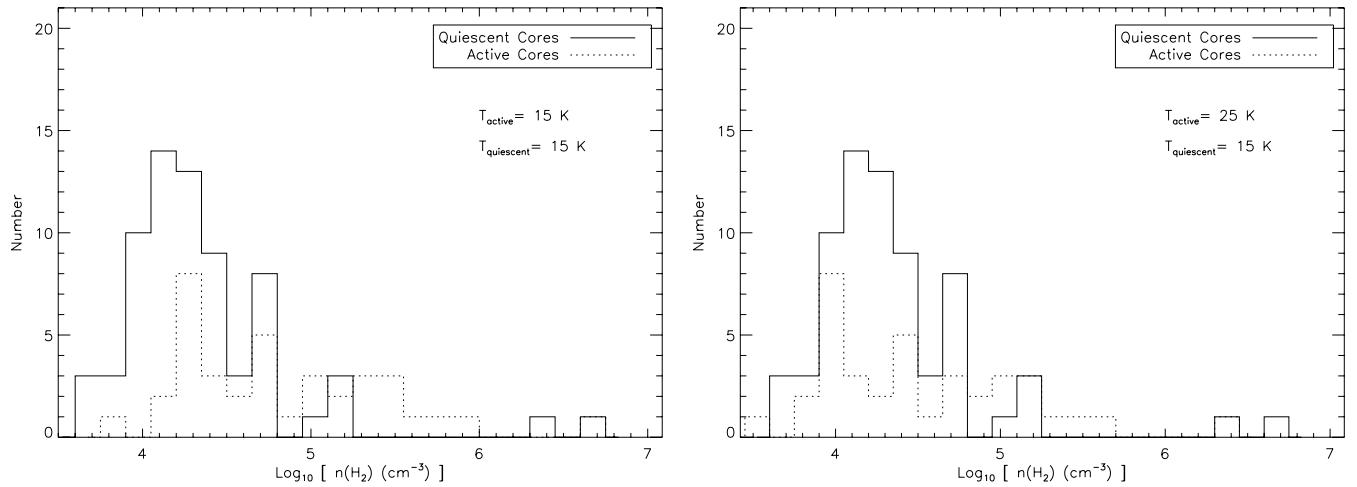

Figure 9. Density histograms of active (dotted line) and quiescent (solid line) cores. Left: the masses and densities of all cores were calculated using a dust temperature of 15 K. The densities of active cores are higher than the densities of quiescent cores, as expected if active cores are collapsing to form stars. The K–S probability that the active and quiescent core density distributions are part of the same parent distribution is 0.04%. Right: the masses and densities of the active cores are calculated using a dust temperature of 25 K, while the masses and densities of the quiescent cores are calculated assuming a dust temperature of 15 K. Even when using the higher dust temperature to calculate the density of active cores, active cores are still denser than quiescent cores. The K–S probability that the active and quiescent cores density distributions are part of the same parent distribution is 6.28%.

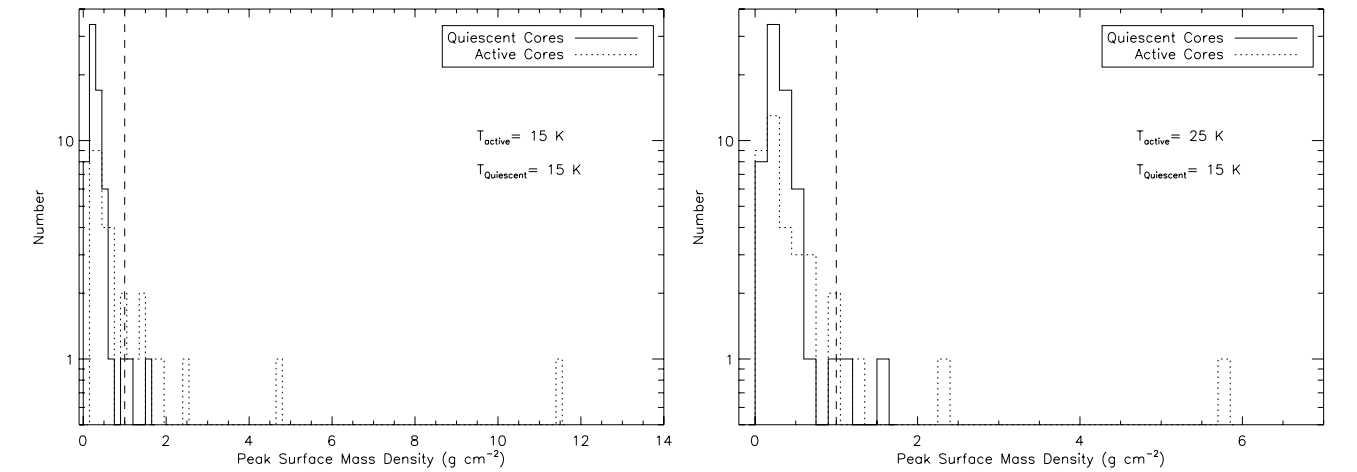

Figure 10. Surface mass density (Σ) histograms of active and quiescent cores. Left: the surface mass densities of the active and quiescent cores were calculated assuming a dust temperature of 15 K. The vertical dashed line at 1 g cm^{-1} marks the value of Σ_{th}. There are two quiescent cores with $\Sigma > \Sigma_{th}$, and 11 active cores with $\Sigma > \Sigma_{th}$. Right: the surface mass densities of the active cores are calculated assuming a dust temperature of 25 K, while the surface mass densities of the quiescent cores are calculated assuming a dust temperature of 15 K. The vertical dashed line at 1 g cm^{-1} marks the value of Σ_{th}. There are three active cores with $\Sigma > \Sigma_{th}$.

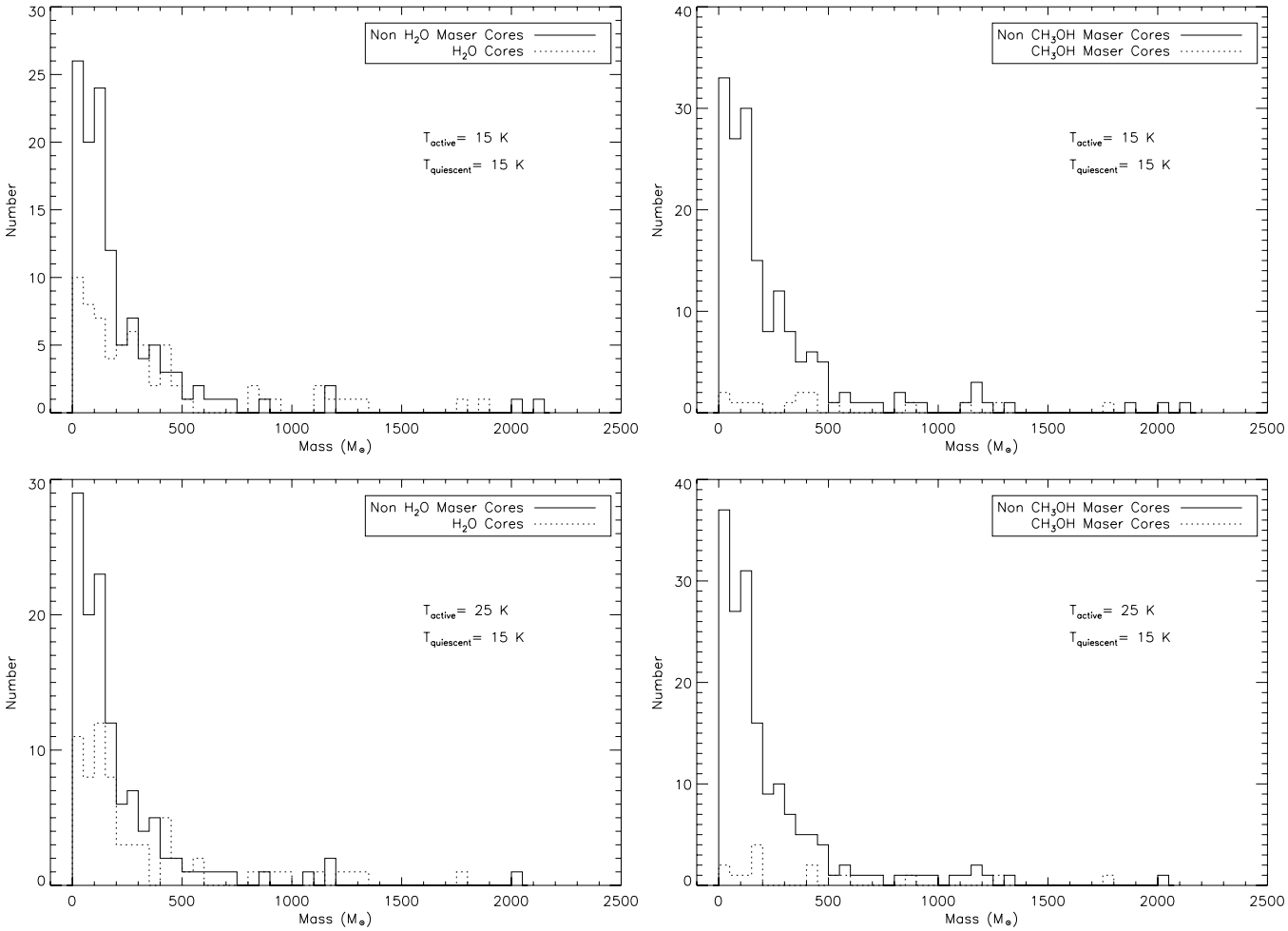

Figure 11. Mass histograms of cores with (dotted line) and without (solid line) H_2O masers (left) and CH_3OH masers (right). When a dust temperature of 15 K to is used to calculate the masses of all cores (top), both H_2O and CH_3OH masers are more likely to be found in high-mass cores than low-mass cores. K–S tests return probabilities of 0.2% and 1.1%, for the H_2O and CH_3OH maser core mass distributions, respectively, that the distributions are drawn from the same parent distribution. Using a dust temperature of 15 K to calculate the masses of quiescent cores, and a dust temperature of 25 K to calculate the masses of active cores (bottom), we still find that massive cores are more likely to contain masers. The K–S test probabilities of the core masses being drawn from the same parent distribution are 11.5% for H_2O and 11.0% for CH_3OH.

5. CONCLUSIONS

We have written an algorithm which finds green fuzzies within the confines of cores within IRDCs (the Green Fuzzy Finder) and determines if a 24 μm point source is associated with the green fuzzy. We employed this algorithm on a sample of 190 cores found toward IRDCs. We classified all of these cores based upon their IR characteristics. Among these classifications are quiescent cores, which show no IR emission, and active cores, which contain green fuzzies and 24 μm point sources. Based on the sizes, densities, as well as H_2O and CH_3OH emission toward active and quiescent cores, we find that active cores are currently forming stars, while quiescent cores appear to be in a preprotostellar phase. We have placed these cores in a hypothetical evolutionary sequence of high-mass star formation in cores within IRDCs.

In our proposed sequence, the active cores are in a later, protostellar phase, while the quiescent cores are in an earlier, preprotostellar phase. The active cores should have smaller sizes, higher densities, and more maser activity than the quiescent cores. All three of these predictions are borne out by the observations. Thus, it appears that our classification scheme reflects a real evolutionary difference between active and quiescent cores. We cannot, however, exclude the possibility that the quiescent cores are also in a protostellar phase, but may contain only faint, low-mass protostars that lie below our current detection limits. In either case, we have established that our classification scheme accurately identifies active, star-forming cores that fall within IRDCs.

As a result of our classification scheme, we have produced a list of high-mass starless core candidates. Further studies of these candidates may help constrain the initial conditions for high-mass star formation.

Our algorithm is based on the IR identification of protostars within the confines of IRDCs. In this paper, we use the mm continuum to identify IRDCs, but for future work we can also use the Catalog of IRDC candidates of Simon et al. (2006a) for this purpose. Because the IR part of our algorithm is based solely on emission available in the GLIMPSE and MIPSGAL Surveys, and because we have already identified IRDCs within the Galactic plane, we can identify protostars within IRDCs throughout the entire survey region. We plan to expand our sample of IRDCs from the 38 in this work to ~10,000, the total number of IRDCs in the Simon et al. (2006a) IRDC Catalog included the GLIMPSE and MIPSGAL regions. We can combine these results with molecular line surveys, such as the

GRS, to establish kinematic distances to, and thus luminosities of protostars within IRDCs across the Galactic plane. This algorithm is an important new tool which will allow us to study the star formation characteristics of a large sample of IRDCs, as well as to establish their role in Galactic star formation.

The authors gratefully acknowledge funding support through NSF grant AST-0098562. This work is based in part on observations made with the *Spitzer Space Telescope*, which is operated by the Jet Propulsion Laboratory, California Institute of Technology under NASA contract 1407. Support for this work was provided by NASA through contracts 1264028 and 1289760 issued by JPL/Caltech, as well as through GSSP06-0007 from the NRAO. The GBT is operated by the National Radio Astronomy Observatory, a facility of the National Science Foundation operated under cooperative agreement by Associated Universities Inc. This works makes use of data from the GLIMPSE and MIPSGAL surveys. We thank the GLIMSPE and MIPSGAL teams for their help and support. The authors also thank the anonymous referee, whose comments and suggestions resulted in a much improved paper.

Facilities: Spitzer, GBT, IRAM:30m.

APPENDIX A

THE GREEN FUZZY FINDER ALGORITHM

The GFF is an automated algorithm which identifies regions of extended, enhanced 4.5 μm emission within the 3σ contours of 1.2 mm continuum emission toward IRDCs. The GFF incorporates color, size, and minimum detection criteria to identify green fuzzies (see Figure 12 for a flowchart of the algorithm).

The first step of the algorithm is to identify regions of at least nine contiguous pixels with values $\geqslant$ 1.8 in a 4.5 μm to 3.6 μm IRAC ratio image. We begin by generating the ratio image, then use Clumpfind2d (Williams et al. 1994) to identify contiguous pixels with values $\geqslant$ 1.8. We thoroughly examined color space, and determined that the empirical value of 1.8 selected most green fuzzies identified by eye, while minimizing the number of spurious detections.

The 4.5 μm to 3.6 μm IRAC ratio image is used in the first step of the GFF because the background levels in the 3.6 μm and 4.5 μm images are very similar ($\sim$1–2 MJy sr^{-1}) and thus, no background subtraction is necessary to compare emission at these wavelengths. In addition, Clumpfind2d identifies relatively few objects in the 4.5 μm to 3.6 μm ratio image, allowing the program to run quickly. When a 4.5 μm to 5.8 μm or 4.5 μm to 8.0 μm ratio image is used, many more objects are identified (a majority of which are not green fuzzies), and the program runs much more slowly.

Because the green fuzzies are typically extended, we we require the GFF to find objects having at least nine contiguous pixels, ensuring that they are well resolved by IRAC. Extincted stars may also appear green in these 3-color images, but because the IRAC PSF is $\sim$2″, they typically have $\sim$4 or fewer pixels and are unlikely to be found by the GFF.

Because some objects other than green fuzzies meet the criteria described above, we require that green fuzzies meet additional color requirements so that the GFF does not spuriously find red objects (e.g., H II regions) or blue objects (e.g., foreground stars). This is done by using flux ratios of the 4.5 μm band with the 5.8 μm and 8.0 μm bands. In order to be a green fuzzy, each candidate must have a mean 4.5 μm to 5.8 μm flux ratio $\geqslant$ 0.40 and a mean 4.5 μm to 8.0 μm flux ratio of $\geqslant$ 0.45. These empirical colors, in combination with the 4.5 μm to 3.6 μm flux ratio of 1.8, select only green objects, thereby excluding objects of other colors.

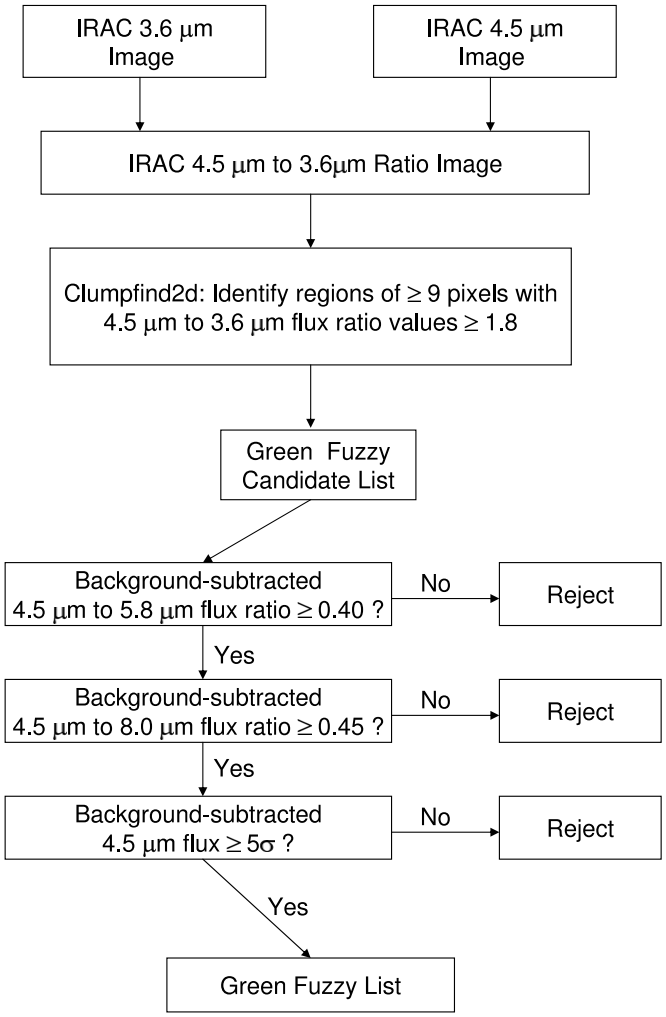

Figure 12. Flowchart of the Green Fuzzy Finder algorithm. Using this algorithm to search within 190 cores, we find 57 green fuzzies. We use GLIMPSE mosaics for our IRAC images.

The determination of the 4.5 μm to 5.8 μm and 4.5 μm to 8.0 μm flux ratios requires background subtraction because the background flux values at 5.8 μm and 8.0 μm are much higher ($\sim$10–15 and $\sim$35–40 MJy sr^{-1}, respectively) than at 4.5 μm. Removing the background from all bands allows for a meaningful color determination, preventing, for example, emission at 8.0 μm from dwarfing emission in the other IRAC bands, rendering all objects red. This method will also remove any smoothly varying foreground emission generated between the IRDCs and the telescope; for simplicity's sake, we will refer to all subtracted emission as background emission.

When determining a background value, it is desirable to use the pixels closest to the green fuzzy candidates. As distance from the edge of the green fuzzy candidate increases, the pixel values remain low while within the IRDC, then increase quickly as the edge of the IRDC is reached. Using the lower values found within the IRDC is critical in estimating an accurate background value. Also, green fuzzies have a wide range of shapes and sizes, so any background estimate must take this into account. Because of these reasons, a simple aperture photometry

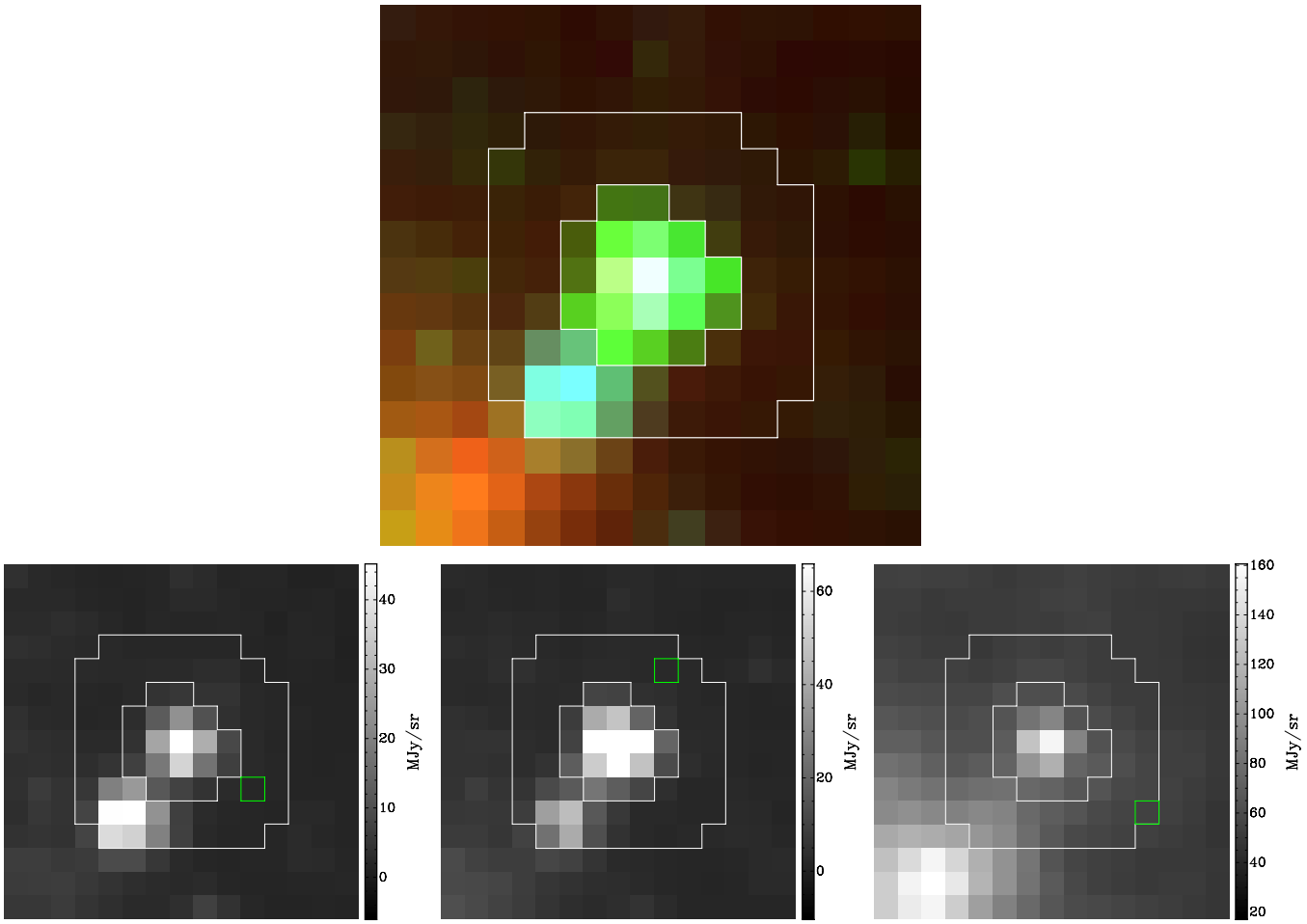

Figure 13. Top: an IRAC 3-color image (8.0 μm in red, 4.5 μm in green, 3.6 μm in blue) of a green fuzzy. The inner contour marks the boundary of the green fuzzy. The outer contour marks a 2-pixel wide region surrounding the green fuzzy. The pixels between the inner and outer contours are used in calculating the background for the green fuzzy. Bottom: IRAC 3.6 μm (left), 4.5 μm (center), and 8.0 μm (right) images of the same green fuzzy. In each of the bottom images, the value of the pixel within the green contour is used as the background for that band.

background determination is insufficient, and the following method is employed.

The background value in each band is found by (1) identifying a 2 pixel wide region of pixels surrounding the green fuzzy, (2) sorting all of the values in this surrounding region, and (3) selecting the value at which 30% of the sorted pixel values are lower. See Figure 13 for a visual representation of this process.

The 4.5 μm to 5.8 μm flux ratio is calculated using the following formula:

$$R_{4.5\,\mu m\,/\,5.8\,\mu m} = (F_{4.5\,\mu m} - BG_{4.5\,\mu m})/(F_{5.8\,\mu m} - BG_{5.8\,\mu m}), \quad \text{(A.1)}$$

where R is the final ratio, F is the mean flux value for all pixels within the green fuzzy candidate boundary, and BG is the background value. The 4.5 μm to 8.0 μm flux ratio is found in the same way, using $F_{8.0\,\mu m}$ and $BG_{8.0\,\mu m}$ instead of $F_{5.8\,\mu m}$ and $BG_{5.8\,\mu m}$.

The final step in the GFF algorithm is to ensure that each green fuzzy is a significant detection in the 4.5 μm band. This step makes sure that chance groupings of noise fluctuations are excluded from the final list of green fuzzies. In order to be considered a significant detection, the mean background subtracted value for all pixels in the green fuzzy candidate must be $\geqslant 5\sigma$, where σ is 0.252 MJy sr^{-1}, the 4.5 μm band extended source sensitivity for GLIMPSE as estimated by the online SENS-PET tool. An example of how the GFF works on an individual core is shown in Figure 14.

APPENDIX B

IDENTIFYING RED AND BLUE IRAC CORES

If a core does not contain a green fuzzy, an automated aperture photometry algorithm is used to determine whether it contains bright 3.6 μm (blue) or bright 8.0 μm (red) emission. The center aperture is a circle, centered on the core position, with radius $R = 0.5R_{\rm core}$, where $R_{\rm core}$ is the radius of the core determined by Rathborne et al. (2006). To determine a background value, all of the pixels within $1.25R_{\rm core}$ are sorted, and the background value is the value at which 30% of the sorted values are lower. The background value is then subtracted from the mean pixel value within the center aperture. If the resulting background subtracted value is $\geqslant 25\sigma$ (where σ is 0.370 MJy sr^{-1} in the 8.0 μm band and 0.272 MJy sr^{-1} in the 3.6 μm band, using the online SENS-PET tool) in the 8.0 μm or 3.6 μm band, it is labeled a red or blue core, respectively. If the flux is $\geqslant 25\sigma$ in both bands, the higher flux value is used to determine if the core is considered "red" or "blue." The value of 25σ is used to ensure that the IRAC emission in the core is bright, and not just a chance alignment with a faint foreground star.

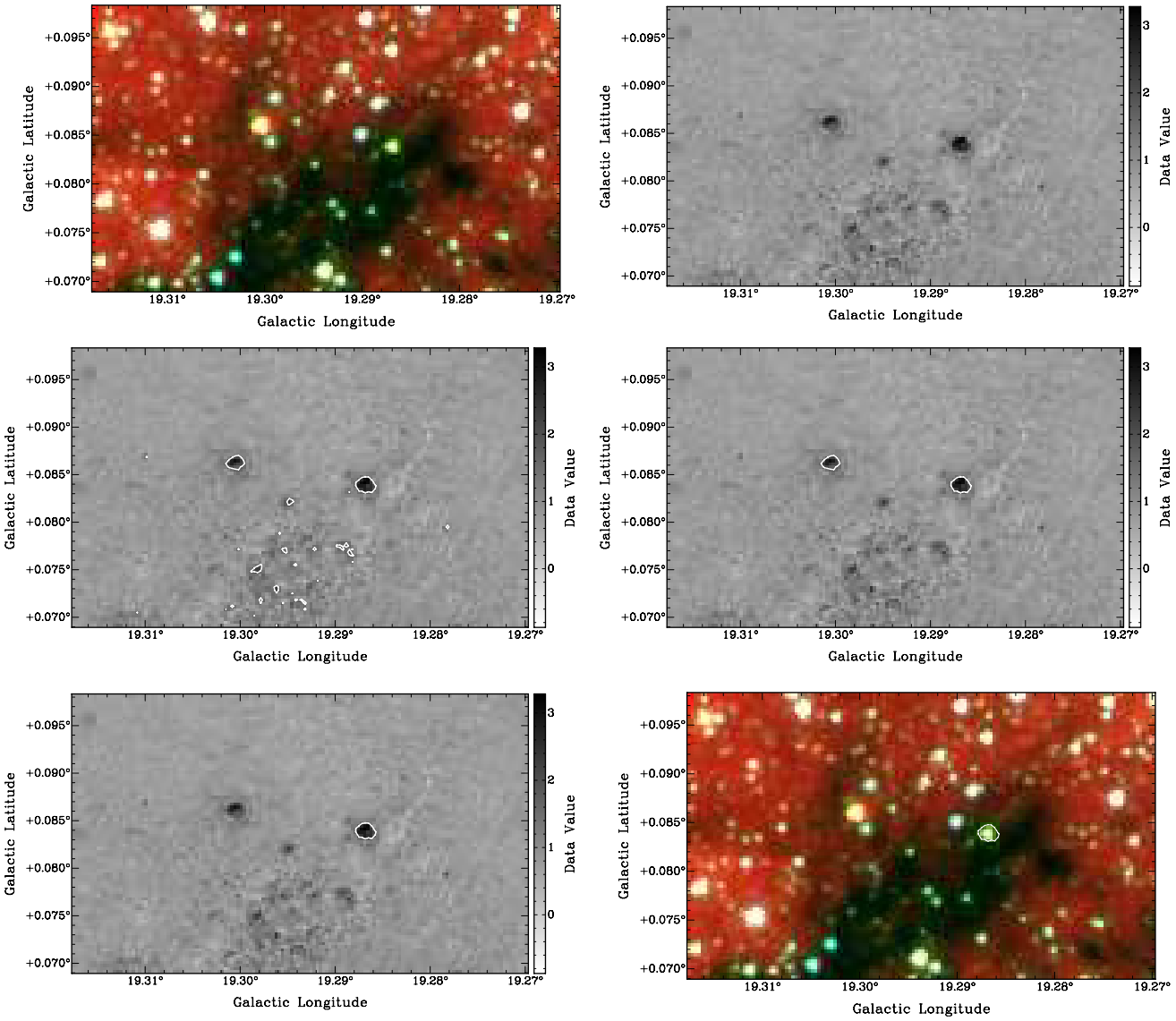

Figure 14. Series of IRAC images of an IRDC which show some of the key steps in the GFF. Top-left: IRAC 3-color image (8.0 μm in red, 4.5 μm in green, 3.6 μm in blue) of an IRDC. Top-right: IRAC ratio image (4.5 μm/3.6 μm) of the same IRDC. Middle-left: IRAC ratio image (4.5 μm/3.6 μm) of the IRDC with contours at the value of 1.8 (the value used to define a green fuzzy in the GFF). In addition to a large green object and a large red object, many small regions have ratio values of at least 1.8. Middle-right: IRAC ratio image (4.5 μm/3.6 μm) of the IRDC with contours around regions with a 4.5 μm/3.6 μm$\geqslant$ 1.8 and at least 9 pixels. Only two objects remain, one red and one green. Bottom-left: IRAC ratio image (4.5 μm/3.6 μm) of the IRDC with contours of the final GFF results. After the additional color criteria (mean 4.5 μm/5.8 μm $\geqslant$ 0.40 and mean 4.5 μm/8.0 μm$\geqslant$ 0.45) of the GFF are applied, the red object is eliminated and only one green fuzzy is found in the IRDC. Bottom-right: IRAC 3-color image (8.0 μm in red, 4.5 μm in green, 3.6 μm in blue) of the IRDC with a contour marking the position and size of the green fuzzy.

APPENDIX C

IDENTIFYING 24 μM POINT SOURCES

Aperture photometry is used to determine 24 μm flux values for each green fuzzy or core. The pixel with the highest 24 μm value within the green fuzzy or within 0.5$R_{\rm core}$ is used as the center of the aperture. An aperture with a radius of 5″ is used to determine the mean 24 μm flux, and the background is found using an annulus with an inner radius of 5″ and an outer radius of 15″. If the background subtracted flux is $\geqslant 20\sigma$ (where σ is 0.124 mJy or 0.207 mJy for the MIPS raster map images and MIPSGAL images, respectively), then the green fuzzy or core is determined to have a 24 μm source. Once the sources are identified, they are individually examined by eye to determine if they are point-like or extended.

REFERENCES

Alves, J., Lombardi, M., & Lada, C. J. 2007, A&A, 462, L17
Behrend, R., & Maeder, A. 2001, A&A, 373, 190
Benjamin, R. A., et al. 2003, PASP, 115, 953
Beuther, H., Sridharan, T. K., & Saito, M. 2005, ApJ, 634, L185
Carey, S. J., Clark, F. O., Egan, M. P., Price, S. D., Shipman, R. F., & Kuchar, T. A. 1998, ApJ, 508, 721
Carey, S. J., Feldman, P. A., Redman, R. O., Egan, M. P., MacLeod, J. M., & Price, S. D. 2000, ApJ, 543, L157
Carey, S. J., et al. 2005, Bull. Am. Astron. Soc., 37, 1252
Clemens, D. P. 1985, ApJ, 295, 422
Draine, B. T. 2003, ARA&A, 41, 241
Egan, M. P., Shipman, R. F., Price, S. D., Carey, S. J., Clark, F. O., & Cohen, M. 1998, ApJ, 494, L199
Enoch, M. L., Evans, N. J., II, Sargent, A. I., Glenn, J., Rosolowsky, E., & Myers, P. 2008, ApJ, 684, 1240
Fazio, G. G., et al. 2004, ApJS, 154, 10
Garay, G., & Lizano, S. 1999, PASP, 111, 1049

Garwood, R., Braatz, J., Marganian, P., & Radziwill, N. 2005, Bull. Am. Astron. Soc., 37, 1212
Hennebelle, P., Pérault, M., Teyssier, D., & Ganesh, S. 2001, A&A, 365, 598
Indebetouw, R., et al. 2005, ApJ, 619, 931
Jackson, J. M., et al. 2006, ApJS, 163, 145
Kalenskiĭ, S. V., Promyslov, V. G., Slysh, V. I., Bergman, P., & Winnberg, A. 2006, Astron. Rep., 50, 289
Krumholz, M. R., & McKee, C. F. 2008, Nature, 451, 1082
Lada, C. J., & Lada, E. A. 2003, ARA&A, 41, 57
Lis, D. C., & Carlstrom, J. E. 1994, ApJ, 424, 189
Marston, A. P., et al. 2004, ApJS, 154, 333
McKee, C. F., & Tan, J. C. 2002, Nature, 416, 59
Miller, G. E., & Scalo, J. M. 1979, ApJS, 41, 513
Minier, V., Ellingsen, S. P., Norris, R. P., & Booth, R. S. 2003, A&A, 403, 1095
Motte, F., Schilke, P., & Lis, D. C. 2003, ApJ, 582, 277
Myers, P. C., & Benson, P. J. 1983, ApJ, 266, 309
Myers, P. C., & Fuller, G. A. 1992, ApJ, 396, 631
Noriega-Crespo, A., et al. 2004, ApJS, 154, 352
Osorio, M., Lizano, S., & D'Alessio, P. 1999, ApJ, 525, 808
Perault, M., et al. 1996, A&A, 315, L165
Pillai, T., Wyrowski, F., Menten, K. M., & Krügel, E. 2006, A&A, 447, 929
Rathborne, J. M., Jackson, J. M., Chambers, E. T., Simon, R., Shipman, R., & Frieswijk, W. 2005, ApJ, 630, L181
Rathborne, J. M., Jackson, J. M., & Simon, R. 2006, ApJ, 641, 389
Rathborne, J. M., Jackson, J. M., Zhang, Q., & Simon, R. 2008, ApJ, 689, 1141
Rathborne, J. M., Simon, R., & Jackson, J. M. 2007, ApJ, 662, 1082
Redman, R. O., Feldman, P. A., Wyrowski, F., Côté, S., Carey, S. J., & Egan, M. P. 2003, ApJ, 586, 1127
Rieke, G. H., et al. 2004, ApJS, 154, 25
Simon, R., Jackson, J. M., Rathborne, J. M., & Chambers, E. T. 2006a, ApJ, 639, 227
Simon, R., Rathborne, J. M., Shah, R. Y., Jackson, J. M., & Chambers, E. T. 2006b, ApJ, 653, 1325
Walsh, A. J., Bertoldi, F., Burton, M. G., & Nikola, T. 2001, MNRAS, 326, 36
Wang, Y., Zhang, Q., Rathborne, J. M., Jackson, J., & Wu, Y. 2006, ApJ, 651, L125
Ward-Thompson, D., Scott, P. F., Hills, R. E., & Andre, P. 1994, MNRAS, 268, 276
Williams, J. P., deGeus, E. J., & Blitz, L. 1994, ApJ, 428, 693
Zinnecker, H., & Yorke, H. W. 2007, ARA&A, 45, 481